EUROPEAN JOURNAL OF COMPUTATIONAL MECHANICS, 2015
VOL. 24, NO. 5, 171–209
http://dx.doi.org/10.1080/17797179.2015.1096229

Taylor & Francis
Taylor & Francis Group

The wavelet finite element method in the dynamic analysis of a functionally graded beam resting on a viscoelastic foundation subjected to a moving load

Mutinda Musuva and Cristinel Mares

Department of Mechanical, Aerospace & Civil Engineering, College of Engineering, Design and Physical Sciences, Brunel University London, England, UK

ABSTRACT

Over recent years there has been a growing demand for materials that possess a wide variation of constitutive properties, which may not naturally occur within homogeneous materials. The evolution of composite materials has led to the development of a relatively new class, commonly referred to as functionally graded materials, which consist of two or more materials (often metals and ceramics) with properties varying continuously with respect to spatial coordinates. In this paper, the dynamic response of a functionally graded (FG) beam is analysed using the wavelet finite element method (WFEM). The scaling functions of the Daubechies wavelet and B-spline wavelet on the interval (BSWI) families are employed as interpolating functions for the construction of the wavelet-based FG beam elements; based on Euler Bernoulli beam theory. The FG beam, comprising of steel and alumina, is assumed to vary continuously in the transverse and axial directions according to the power law. The free vibrations behaviour of a FG beam with different material distributions is compared with other approaches from published data to validate and assess the performance of this formulation. A FG beam resting on a viscoelastic foundation is analysed when subjected to a moving point load. The dynamic responses are evaluated using the Newmark time integration method. The effects of the material distribution, velocity of the moving load and damping of the system are discussed based on the numerical examples presented. The results indicate that WFEMs achieve higher levels of accuracy with fewer elements implemented, in comparison to the classical finite element method, in the analysis of the FG beam. Furthermore, the BSWI wavelet-based approach performs better than the Daubechies-based WFEM.

ARTICLE HISTORY
Received 31 July 2015
Accepted 16 September 2015

KEYWORDS
Functionally graded beam; wavelet finite elements; Daubechies wavelet; connection coefficients; B-spline wavelet on the bound interval; moving load

CONTACT Cristinel Mares cristinel.mares@brunel.ac.uk

1. Introduction

Research efforts and advancements in the fabrication and application of composite materials in various engineering fields have recently intensified. This is of significance due to the growing need for materials that simultaneously possess a wide variation of material properties, which may not naturally occur within homogeneous materials. For instance in the aerospace and automotive industries, the need for light-weight materials that possess high strength to weight ratios and stiffness to weight ratios has led to the fabrication and application of some composite materials that combine two or more materials varying in properties. However, some composite materials are subject to high localised stress concentration and discontinuous stress distribution in areas where there is an abrupt change in material properties. For example, laminate composites when subjected to extreme loading conditions may be susceptible to initiation and further propagation of cracks resulting in delamination or failure of the composite material (Jha, Kant, & Singh, 2013). Further research has been carried out to mitigate some of these limitations leading to a relatively new class of composite materials known as functionally graded materials (FGM). FGMs were conceptualised in the mid-1980s by a faction of material scientists in Japan (Koizumi, 1997) and consist of two or more materials (often metals and ceramics) with different properties that vary continuously in the desired spatial direction(s). The ceramic materials offer high stiffness, low density, good thermal resistance and corrosion resistance while the metals improve the strength and toughness of the FGM. The material composition and variation can be tailored to achieve the target properties for advanced materials. Furthermore, FGMs may be used as an adhesive between different materials of structures that may be simultaneously subjected to different loading environments. It is for these reasons that the popularity of FGMs is vastly growing for different engineering applications in the automotive, aerospace, nuclear, biomedical and electronic and defence industries just to name a few. Therefore, research has been undertaken in order to understand and predict their behaviour when subjected to various loading environments, such as mechanical, thermal, electrical or in some cases a combination of loading conditions.

Considerable advancements in research of functionally graded (FG) plates and shells have been carried out (Jha et al., 2013), although literature focused on the dynamic response of FG beams is still limited. Nonetheless, the need to analyse the behaviour of FG beams is rapidly growing for both practical and theoretical purposes. The thermoelastic behaviour of FG beams was investigated by Chakraborty, Gopalakrishnan and Reddy (2003), who implemented a new exact shear deformable FG beam finite element formulation based on the Timoshenko beam theory. Aydogdu and Taskin (2007) compared free vibration of short FG beams using the Euler-Bernoulli, parabolic shear deformation and exponential shear deformation beam theories. Kadoli, Akhtar and Ganesan (2008) applied the classical finite element method (FEM) to analyse the static deflection and stresses

of a transversely varying FG beam, based on higher order shear deformation theory and power law of gradation. Pradhan and Chakraverty (2013) compared the natural frequencies of a Euler Bernoulli FG beam with a Timoshenko FG beam based on the Rayleigh-Ritz method. The classical FEM was also implemented by Alshorbagy, Eltaher and Mahmoud (2011) to analyse the free vibration of a Euler Bernoulli FG beam. Further research has been carried out to investigate the dynamic response of FG beams subjected to moving loads. Simsek and Kocaturk (2009) analysed the free vibration and dynamic response of a Euler-Bernoulli FG beam subjected to a concentrated moving harmonic load. Simsek (2010a) extended this research by investigating the dynamic response of the FG beam subjected to a moving mass based on classical, first-order shear deformation and third-order shear deformation beam theories. Simsek (2010b) also analysed the non-linear dynamic behaviour of a transversely varying Timoshenko FG beam subjected to a moving harmonic load. Khalili, Jafari and Eftekhari (2010) investigated the dynamic response of a simply supported FG beam subjected to a moving load by combining the Rayleigh-Ritz method and the differential quadrature method.

The need for more efficient, effective and accurate mathematical tools to analyse various engineering problems has resulted in the formulation of different analytical, semi-analytical and numerical approaches. In structural analysis, one such approach that has been recently developed is the wavelet-based finite element method. The method involves combining wavelet analysis with the classical FEM by utilising the wavelet and scaling functions as interpolating functions, thus providing an alternative to the conventional polynomial interpolation functions used in FEM. The method offers vast potential for the accurate and efficient analysis of complex structural problems through the implementation of multiresolution analysis (MRA) which allows for the alteration of the scale of a local wavelet finite element (WFE). This is advantageous since the accuracy of the solution, particularly in areas with high gradients and singularities present, can be greatly improved locally. Furthermore, computational costs are reduced since fewer elements are required to achieve acceptable levels of accuracy due to rapid convergence of the method (Chen, He, Xiang, & Li, 2006; Xiang, Chen, He, & Dong, 2007). For these reasons, the approach has attracted the attention of researchers over the past decade to formulate and implement WFEM using different wavelet families and analyse various structural static and dynamic problems. Ko, Kurdila and Pilant (1995) developed the Daubechies wavelet-based FEM to solve a 1D and 2D, second-order Neumann problem. Zhou, Wang and Zheng (1998) implemented the wavelet Galerkin FEM to analyse the bending of plates and beams. Ma, Xue, Yang and He (2003) developed a wavelet-based beam finite element which was used to analyse static beam problems. Chen, Yang, Ma and He (2004) developed a two-dimensional Daubechies WFE which was implemented in the analysis of the bending of thin plates. Diaz, Martin and Vampa (2009) formulated a plate based on Mindlin-Reissner plate theory using the Daubechies wavelet family. Chen and Wu (1995) combined the conventional FEM with the accuracy of the

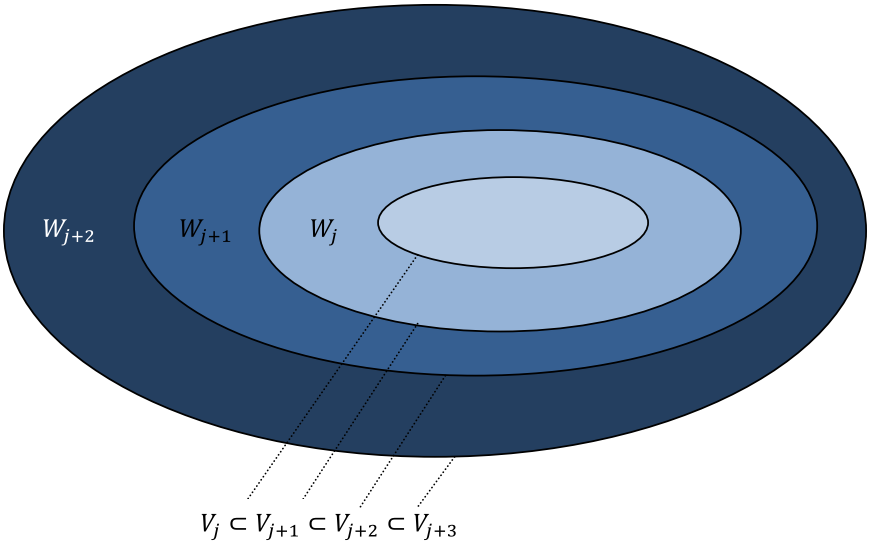

Figure 1. Illustration of multiresolution subspaces V_j and W_j.

spline functions as shape functions for free vibration analysis of frame structures. Xiang, Chen, He and Dong (2007) constructed a range WFEs, which included the axial rod, beam (Timoshenko and Euler Bernoulli), plane bar, spatial bar and plane truss using the B-spline wavelet on bounded interval (BSWI). Yang et al. (2014) used the BSWI-based WFEM to analyse elastic wave propagation for a cracked arch based on Castigliano's theorem and Paris equation. He and Ren (2012) developed a beam WFE based on the trigonometric wavelet for the static analysis of structural problems.

In this paper, the wavelet finite element method (WFEM) is implemented for the analysis of FG beams varying axially and transversely based on the power gradation law. To the best of the author's knowledge, the Daubechies and the BSWI wavelet families are for the first time used to construct the FG beam WFEs based on Euler-Bernoulli beam theory and are compared with the classical FEM via numerical examples. In Section 2 of this paper, a brief introduction into general wavelet theory and MRA is presented. The Daubechies wavelet and BSWI wavelet families are also discussed and the evaluation of the multiscale connection coefficients is highlighted. The construction of the FG wavelet-based beam element is presented in Section 3 based on the power law. Numerical examples are presented in Section 4 to validate and compare the performance of the different approaches. Furthermore, a free vibration analysis of a simply supported beam is presented and the dynamic response of a FG beam subjected to a moving point load is highlighted. The effects of varying the material distribution, velocity of the moving load and damping of the system on the dynamic responses of the beam are discussed; followed by conclusions.

2. Wavelet analysis and multiresolution

Wavelets are described as a class of basis functions that represent functions locally; both in space (frequency) and time. Furthermore, wavelets allow for analysis of functions or data to be carried out at different resolutions (scales) (Strang, 1989). The wavelet basis emanates from a set of wavelet coefficients associated at a particular location in time and exist in different multiresolution scales. In relation to data and frequency, the coefficients at coarse resolution scales are associated with low frequency features. As the resolution scales become finer, more information (detail) is added from the higher resolution coefficients. Therefore, the coefficients at very fine resolution scales are associated with high frequency details that are highly localised (Li & Chen, 2014).

Multiresolution is an advantageous property of wavelets and refers to the simultaneous appearance of multiple scales in function decompositions in the Hilbert space $L^2(\mathbb{R})$ using a sequence of closed subspaces V_j; which satisfy the conditions (Ko et al., 1995):

$$\cdots V_{-2} \subset V_{-1} \subset V_0 \subset V_1 \subset V_2 \subset \ldots \tag{1}$$

$$\overline{\bigcup_{j\in\mathbb{Z}} V_j} = L^2(\mathbb{R}) \tag{2}$$

$$\bigcap_{j\in\mathbb{Z}} V_j = \{0\} \tag{3}$$

$$\begin{aligned} &f_2(x) = f(2x) \forall x \\ &f \in V_j \leftrightarrow f_2 \in V_{j+1} \quad j \in \mathbb{Z} \end{aligned} \tag{4}$$

$$\begin{aligned} &f_n(x) = f(x-n) \\ &f \in V_0 \leftrightarrow f_n \in V_0 \qquad n \in \mathbb{Z} \end{aligned} \tag{5}$$

The orthogonal complement subspace W_j of V_j contains the additional "detail" for subspace V_{j+1}:

$$V_{j+1} = V_0 \oplus W_0 \oplus W_1 \oplus W_2 \cdots \oplus W_j \tag{6}$$

and the space $L^2(\mathbb{R})$ can be represented as a direct sum as illustrated in Figure 1:

$$V_{j+1} = V_j \oplus W_j \tag{7}$$

Let the scaling function of the MRA $\phi \in L^2(\mathbb{R})$. Thus, the orthonormal basis of V_j is defined as:

$$\phi_k^j(x) = 2^{\frac{j}{2}}\phi(2^j x - k) \quad k \in \mathbb{Z} \tag{8}$$

Given that the above properties in Equations (1) and (7) are satisfied, there exists a wavelet function $\psi \in L^2(\mathbb{R})$ to which the wavelet orthonormal basis for subspace W_j at scale j are defined as:

$$\psi_k^j(x) = 2^{\frac{j}{2}}\psi(2^j x - k) \quad k \in \mathbb{Z} \tag{9}$$

The scaling $\phi(x)$ and wavelet functions $\psi(x)$ correspond to the subspaces V_j and W_j, respectively. The wavelet space W_j represents the difference between current subspace V_j and subsequent subspace V_{j+1}. Consequently, each W_j becomes automatically orthogonal to all other W_j for $k < j$ due to the inclusion in and orthogonality to V_j.

For the fundamental space V_0, the scaling function $\phi(x)$ and its translates $\phi(x-k)$ produce an orthonormal basis for V_0. The orthonormal basis for the next space V_1 is the rescaled function $\sqrt{2}\phi(2x-k)$. Therefore, at scaling level j, V_j has the basis $\phi_{jk}(x) = \{2^{j/2}\phi(2^j x - k)\}$, while the detail space W_j is formed by the dilation and translation of the wavelet function $\psi_{jk}(x) = \{2^{j/2}\psi(2^j x - k)\}$. The projections of a function $f \in L^2(\mathbb{R})$ at scale j in the subspaces V_j and W_j defined as $P_j f$ and $Q_j f$, respectively, are expressed as:

$$P_j f = \sum_k a_k^j \phi_k^j(x) \tag{10}$$

$$Q_j f = \sum_k b_k^j \psi_k^j(x) \tag{11}$$

where a_k^j and b_k^j are coefficients in the subspaces V_j and W_j, respectively.

2.1. Daubechies wavelet

The Daubechies family of wavelets developed by Ingrid Daubechies (1988) have the properties of compact supported orthonormal wavelets. The Daubechies scaling and wavelet functions for family of order L are described by the "two scale" relations:

$$\phi_L(x) = \sum_{k=0}^{L-1} p_L(k)\phi_L(2x-k) \tag{12}$$

$$\psi_L(x) = \sum_{k=0}^{L-1} q_L(k)\phi_L(2x-k) \tag{13}$$

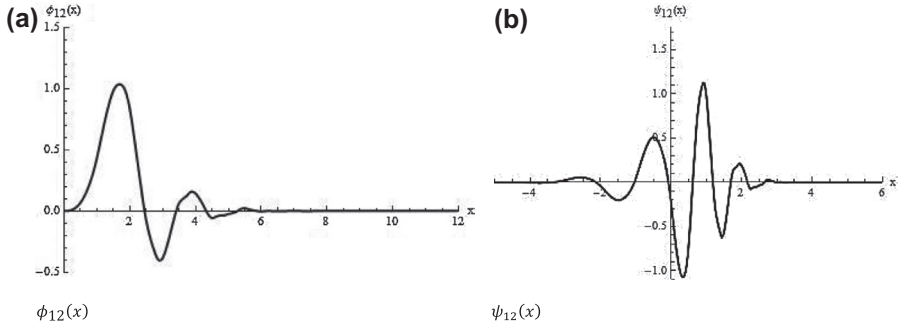

Figure 2. The Daubechies (a) scaling and (b) wavelet functions of order $L = 12$.

The normalised wavelet function filter coefficients $q_L(k)$ and scaling function filter coefficients $p_L(k)$ have the relation $q_L(k) = (-1)^k p_L(1-k)$.

The supports of the scaling and wavelet functions are $[0, L-1]$ and $[1-\frac{L}{2}, \frac{L}{2}]$, respectively. An example of the Daubechies scaling and wavelet functions of order $L = 12$ are presented in Figures 2(a) and 2(b), respectively.

The Daubechies wavelets possess the following properties (Daubechies, 1988):

$$\int_{-\infty}^{\infty} \phi_L(x)\,\mathrm{d}x = 1 \tag{14}$$

$$\int_{-\infty}^{\infty} \phi_L(x-k)\phi_L(x-l)\,\mathrm{d}x = \delta_{k,l} \tag{15}$$

$$\int_{-\infty}^{\infty} \phi_L(x)\psi_L(x-k)\mathrm{d}x = 0 \tag{16}$$

$$\int_{-\infty}^{\infty} x^m \psi_L(x)\mathrm{d}x = 0 \quad m = 0, 1, \ldots, \frac{L}{2} - 1 \tag{17}$$

From the property given in Equation (17), the Daubechies wavelets have $\frac{L}{2} - 1$ vanishing moments and therefore, the scaling functions can represent any polynomial of order equal to but not greater than $\frac{L}{2} - 1$; so that for each m, there exists a set of constants c_k^m with the property:

$$\sum_k c_k^m \phi_L(x-k) = x^m \tag{18}$$

2.2. Connection coefficients

In the case of some wavelet families such as the Daubechies wavelet, the scaling and wavelet functions have no explicit expression. Furthermore, the derivatives of the scaling functions are highly oscillatory, particularly for the low order wavelet families and/or the high order derivatives. This implies that the integrals cannot be evaluated directly in closed form and require the computation of what is commonly referred to as connection coefficients (Latto, Resnikoff, & Tenenbaum, 1991). Implementing the Daubechies wavelet family in the formulation of the wavelet-based finite element of the FG beam requires the evaluation of the two-term connection coefficient defined as:

$$ {}_{a,b}\Gamma_{k,l}^{j,d_1,d_2} = 2^j \int_{-\infty}^{\infty} \mathcal{X}_{[0,1]}(\xi)\phi_a^{(d_1)}(2^j\xi - k)\phi_b^{(d_2)}(2^j\xi - l)\mathrm{d}\xi \tag{19} $$

where a and b are the orders of the scaling function of the Daubechies wavelets at multiresolution j. The values d_1 and d_2 denote the order of the derivative of the scaling functions. $\mathcal{X}_{[0,1]}(x)$ is the characteristic function:

$$ \mathcal{X}_{[0,1]}(x) = \begin{cases} 1 & 0 \le x \le 1 \\ 0 & \text{otherwise} \end{cases} \tag{20} $$

and satisfies the "two-scale" relation

$$ \mathcal{X}_{[0,1]}\left(\frac{\gamma}{2}\right) = \mathcal{X}_{[0,1]}(\gamma) + \mathcal{X}_{[1,2]}(\gamma) = \mathcal{X}_{[0,1]}(\gamma) + \mathcal{X}_{[0,1]}(\gamma - 1) \tag{21} $$

The formulation presented is a modified algorithm of that derived by Chen, He, Xiang and Li (2006). According to the two scale relation of the scaling function in Equation (12),

$$ \phi_L(2^j\xi - k) = \sum_r p(r)\phi_L\left(2^{j+1}\xi - 2k - r\right) \tag{22} $$

Furthermore, differentiating Equation m times,

$$ 2^{jm}\phi_L^{(m)}(2^j\xi - k) = 2^{(j+1)m}\sum_r p(r)\phi_L^{(m)}\left(2^{j+1}\xi - 2k - r\right) \tag{23} $$

Substituting Equation (23) into Equation (19) for derivatives of order d_1 and d_2, respectively.

$$ \begin{aligned} {}_{a,b}\Gamma_{k,l}^{j,d_1,d_2} = 2^j \int_{-\infty}^{\infty} \mathcal{X}_{[0,1]}(\xi)2^{d_1}\sum_r p(r)\phi_a^{(d_1)}\left(2^{j+1}\xi - 2k - r\right)2^{d_2} \\ \sum_s p(s)\phi_b^{(d_2)}(2^{j+1}\xi - 2l - s)\mathrm{d}\xi \end{aligned} \tag{24} $$

Let $2\xi = \gamma$ thus Equation (24) can be expressed as:

$$ {}_{a,b}\Gamma_{k,l}^{j,d_1,d_2} = 2^{j+d_1+d_2} \sum_{r,s} p(r)p(s) \int_{-\infty}^{\infty} \mathcal{X}_{[0,1]}\left(\frac{\gamma}{2}\right) \phi_a^{(d_1)}(2^j\gamma - 2k - r)\phi_b^{(d_2)}(2^j\gamma - 2l - s)\frac{\mathrm{d}\gamma}{2} \tag{25} $$

Substituting Equation (21) into Equation (25) and

$$ \begin{aligned} {}_{a,b}\Gamma_{k,l}^{j,d_1,d_2} = 2^{j+d_1+d_2-1} \sum_{r,s} p(r)p(s) \int_{-\infty}^{\infty} \mathcal{X}_{[0,1]}(\gamma)\phi_a^{(d_1)}(2^j\gamma - 2k - r)\phi_b^{(d_2)} \\ (2^j\gamma - 2l - s)d\gamma + \int_{-\infty}^{\infty} \left[\mathcal{X}_{[0,1]}(\gamma - 1)\phi_a^{(d_1)}(2^j\gamma - 2k - r)\phi_b^{(d_2)}(2^j\gamma - 2l - s)\right]\mathrm{d}\gamma \end{aligned} \tag{26} $$

Following the expression of the connection coefficients as defined in Equations (19) and (26) can be expressed as:

$$ {}_{a,b}\Gamma_{k,l}^{j,d_1,d_2} = 2^{d_1+d_2-1} \sum_{r,s} [p_a(r - 2k)p_b(s - 2l) + p_a\left(r - 2k + 2^j\right)p_b\left(s - 2l + 2^j\right)]\Gamma_{r,s}^{j,d_1,d_2} \tag{27} $$

where $2 - a \le k, r \le 2^j - 1$ and $2 - b \le l, s \le 2^j - 1$. Equation (27) can be expressed in matrix form as:

$$ \begin{aligned} \left((a+2^j-2)(b+2^j-2)\times 1\right)\left\{{}_{a,b}\boldsymbol{\Gamma}^j\right\} = 2^{d_1+d_2-1} \\ \left[{}_{a,b}P\right]_{\left((a+2^j-2)(b+2^j-2)\times 1\right)} \left\{{}_{a,b}\Gamma^j\right\} \end{aligned} \quad \left((a+2^j-2)(b+2^j-2)\times(a+2^j-2)(b+2^j-2)\right) \tag{28} $$

where ${}_{a,b}\Gamma^j$ is a vector of length $\left(\left(a + 2^j - 2\right)\left(b + 2^j - 2\right) \times 1\right)$ containing the connection coefficients, while the square matrix $\left[{}_{\boldsymbol{a,b}}\boldsymbol{P}\right]$ contains the filter coefficients as expressed in Equation (27) with the dimensions $\left(\left(a + 2^j - 2\right)\left(b + 2^j - 2\right) \times \left(a + 2^j - 2\right)\left(b + 2^j - 2\right)\right)$. It is necessary to employ the moment condition of the wavelet functions to formulate the normalising conditions required to generate a sufficient number of inhomogeneous equations so as to uniquely determine the connection coefficients. These additional normalising equations are formulated from the fact the Daubechies scaling functions of order L can exactly represent any polynomial of order m with $0 \le m \le \frac{L}{2} - 1$.

$$ \xi^m = 2^{\frac{j}{2}} \sum_k {}_L M_k^{j,m} \phi_L\left(2^j\xi - k\right) \tag{29} $$

where ${}_L M_k^{j,m}$ are the moments and are expressed as:

$$ {}_L M_k^{j,m} = \int_{-\infty}^{\infty} x^m \phi_{L,k}^j(x)\mathrm{d}x \tag{30} $$

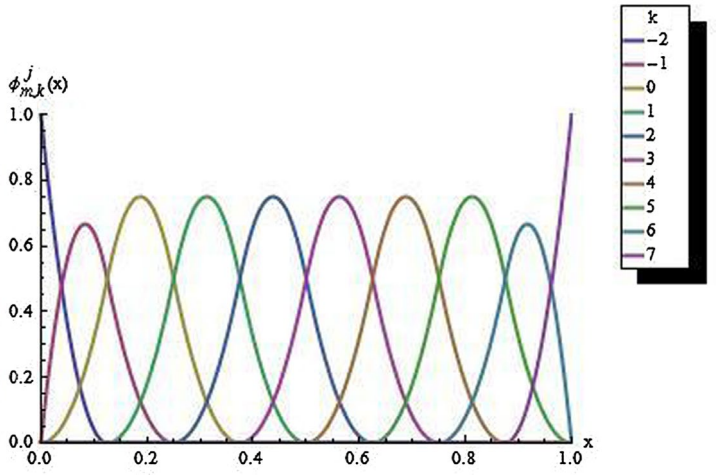

Figure 3. The BSWI scaling function $\boldsymbol{\phi}^3_{3,k}(x)$.

2.3. B-spline wavelets on the interval [0,1] (BSWI)

Given a knot vector t^j_mcomprising of a sequence of knots t^j_i on [0,1], via joining the piecewise polynomials between the knots, one is able to construct B-splines at a scale $j \in \mathbb{N}_0$ (Chui & Quak, 1992). Therefore, the basis functions in subspace V_j for B-splines of order m and scale $j > 0$, are expressed as (Chui & Quak, 1992):

$$B^j_{m,k}(x) = \left(t^j_{k+m} - t^j_k\right)\left[t^j_k, \ldots, t^j_{k+m}\right]_f (t-x)^{m-1}_+ \tag{31}$$

with the knot sequence

$$\begin{gathered} \left\{t^j_k\right\}^{2^j+m-1}_{k=-m+1} \\ t^j_k \le t^j_{k+1} \end{gathered} \tag{32}$$

$\left[t^j_k, t^j_{k+1}, \ldots, t^j_{k+m}\right]_t$, is the mth divided difference of the truncated power function $(t-x)^{m-1}_+$ with respect to variable t. Therefore, the general B-splines in Equation (31) can be expressed as:

$$\begin{gathered} B^j_{m,k}(x) = \frac{x - t^j_k}{t^j_{k+m-1} - t^j_k} B^j_{m-1,k}(x) + \\ \frac{t^j_{k+m} - x}{t^j_{k+m} - t^j_{k+1}} B^j_{m-1,k+1}(x) \qquad B^j_{1,k}(x) = \begin{cases} 1 & k \le x \le k+1 \\ 0 & \text{otherwise} \end{cases} \end{gathered} \tag{33}$$

$$\operatorname{supp} B^j_{m,k}(x) = \left[t^j_k, t^j_{k+m}\right] \tag{34}$$

The B-spline basis of the knot sequence expressed in Equation (32) has m-tuple knots at 0 and 1 and simple knots inside the unit interval. Therefore, for the knot sequence on [0,1], t_k^j is given as (Quak & Weyrich, 1994):

$$t_k^j = \begin{cases} 0 & -m+1 \le k < 1 \\ 2^{-j}k & 1 \le k < 2^j \\ 1 & 2^j \le k \le 2^j + m - 1 \end{cases} \tag{35}$$

The corresponding B-wavelet is given as:

$$\begin{gathered} \psi_{m,k}^j(x) = \frac{1}{2^{m-1}} \sum_{l=0}^{2m-2} (-1)^l N_{2m}(l+1) B_{2m,2i+l}^{j+1,(m)}(x) \\ \operatorname{supp} \psi_{m,k}^j(x) = \left[\frac{k}{2^j}, \frac{k+2m-1}{2^j} \right] \end{gathered} \tag{36}$$

where $N_m(x)$ denotes the cardinal spline of order m. In order to have one inner wavelet on the interval [0,1], the following condition must be met (Quak & Weyrich, 1994):

$$2^{j_0} \ge 2m - 1 \tag{37}$$

where j_0 is the smallest multiresolution scale corresponding to order m that ensures there is at least one inner wavelet on the interval [0,1].

Thus, the scaling functions, $\phi_{m,k}^j(x)$, and corresponding semi-orthogonal wavelet functions, $\psi_{m,k}^j(x)$ of BSWI of order m at scale $j \ge j_0$ are evaluated as follows:

$$\phi_{m,k}^j(x) = \begin{cases} B_{m,k}^{j_0}\left(2^{j-j_0}x\right) & -m+1 \le k \le -1 \\ B_{m,0}^{j_0}\left(2^{j-j_0}x - 2^{-j_0}k\right) & 0 \le i \le 2^j - m \\ B_{m,2^j-k-m}^{j_0}\left(1 - 2^{j-j_0}x\right) & 2^j \le i \le 2^j + m - 1 \end{cases} \tag{38}$$

$$\psi_{m,k}^j(x) = \begin{cases} \psi_{m,k}^{j_0}\left(2^{j-j_0}x\right) & -m+1 \le k \le -1 \\ \psi_{m,0}^{j_0}\left(2^{j-j_0}x - 2^{-j_0}k\right) & 0 \le i \le 2^j - m \\ \psi_{m,2^j-k-2m+1}^{j_0}\left(1 - 2^{j-j_0}x\right) & 2^j \le i \le 2^j + m - 1 \end{cases} \tag{39}$$

Since BSWI scaling functions are expressed explicitly, the derivatives of the scaling functions can be obtained by directly differentiating Equation (38).

$$\phi_{m,k}^{j,(n)}(x) = \frac{\mathrm{d}^n \phi_{m,k}^j(x)}{\mathrm{d}x^n} \tag{40}$$

The scaling function and its translates of the BSWI of order 3 at multiresolution scale 3 are illustrated in Figure 3.

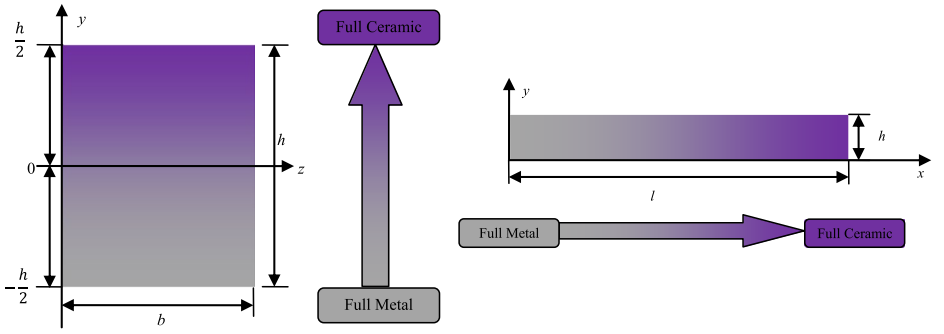

Figure 4. FG beam with (a) transverse gradation and (b) axial gradation.

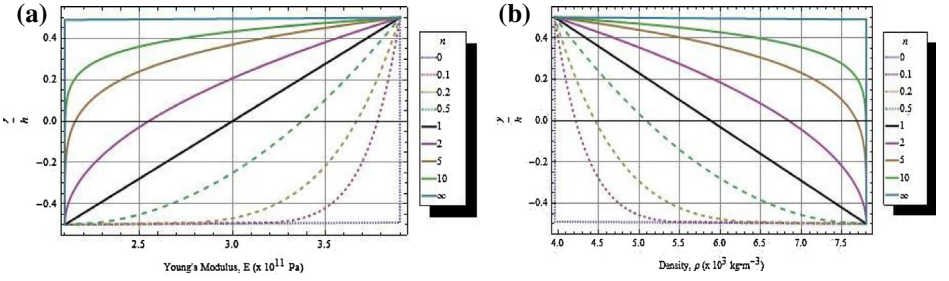

Figure 5. The effective (a) Young's modulus and (b) mass density, through the thickness of a steel-alumina FG beam for different power law exponents *n*.

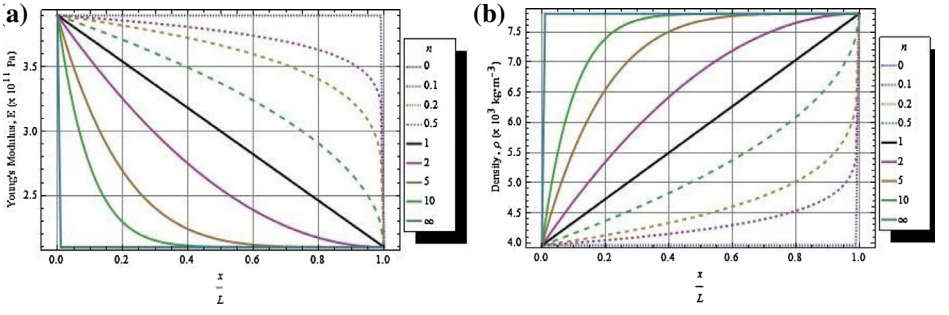

Figure 6. The effective (a) Young's modulus and (b) mass density, along the length of a steel-alumina FG beam for different power law exponents *n*.

3. FGMs theory and formulations

3.1. FGM material gradation

In this study, it is assumed that the constituent materials of the FG beam are a ceramic and a metal which varies continuously along (a) the thickness of the beam in the transverse direction and (b) axially along the length as illustrated in Figure 4. The height of the beam is denoted by *h*, the length *l* and width *b*.

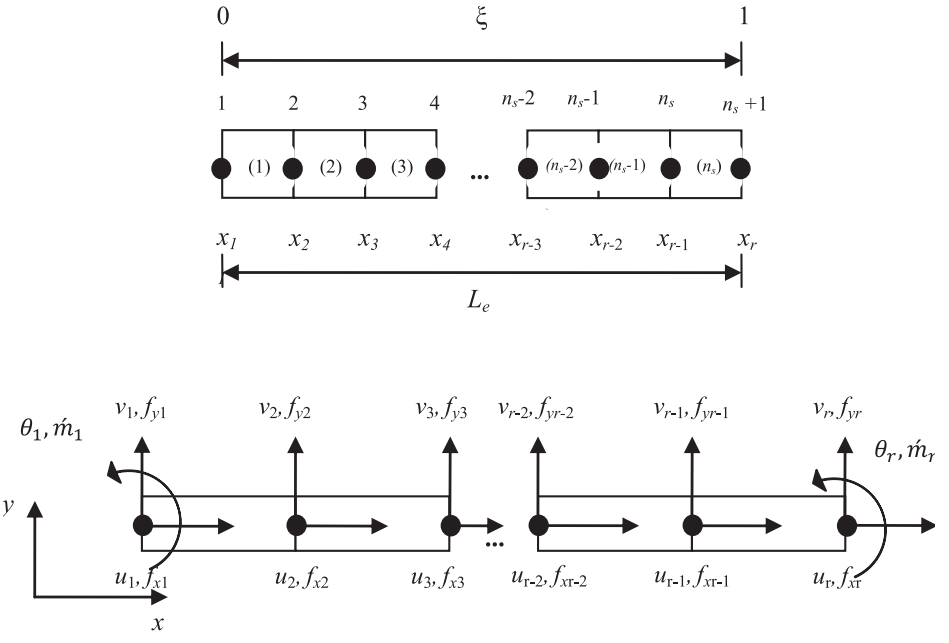

Figure 7. Two-dimensional beam WFE layout.

The upper (a)/left hand (b) and lower (a)/right hand (b) surfaces are assumed to be ceramic and metal, respectively. The variation of the material distribution of the FG beam is described according to the power law introduced by Wakashima, Hirano, and Niino (1990).

In the case of transverse variation of the material properties $P(y)$ of the FG beam, containing the two constituent materials, according to the power gradation law is expressed as (Wakashima et al., 1990):

$$P(y) = P_{\text{lo}}\left(\left[P_{\text{ratio}} - 1\right]\left(\frac{y}{h} + \frac{1}{2}\right)^{n} + 1\right) \tag{41}$$

where P_{ratio} is the ratio of the upper and lower surface material properties P_{u} and P_{lo}, respectively. The effective material properties $P(y)$ for this study include the Young's modulus E and density ρ. The non-negative power law index, which determines the material transverse variation, is denoted by n. The variation of the effective (a) Young's modulus and (b) mass density of a steel-alumina FG beam through the thickness is illustrated in Figure 5.

Similarly, the effective material properties for the axially varying FG beam can be obtained from the expression:

$$P(x) = P_{\text{r}}\left(\left[P_{\text{ratio}} - 1\right]\left(1 - \frac{x}{l}\right)^{n} + 1\right) \tag{42}$$

where P_{ratio} is the ratio of the left end and right end surface material properties P_l and P_r respectively. Figure 6 illustrates the (a) effective Young's modulus and (b) mass density of the axially varying steel-alumina FG beam.

3.2. FGM beam wavelet-based finite element layout

The FG beam is formulated using the WFEM based on the Euler Bernoulli beam theory, with axial and bending deformation as well as loading effects taken into consideration. The layout selected for the WFE of length L_e has the axial and transverse displacement degrees of freedom (DOFs) at each elemental node and the rotation DOFs only at the elemental end nodes as presented in Figure 7. Each WFE contains r number of elemental nodes, n_s number of elemental segments and a total number of s DOFs. The axial and transverse displacements are approximated using the wavelet scaling functions. For a particular multiresolution scale j, the axial and transverse displacements at any point in natural coordinates $\xi = \frac{x-x_1}{L_e}$ $(0 \le \xi \le 1)$, are given as:

$$\begin{aligned} u(\xi) &= \sum_{k=h}^{2^j-1} a^j_{z-2,k} \phi^j_{z-2,k}(\xi) \\ v(\xi) &= \sum_{k=i}^{2^j-1} b^j_{z,k} \phi^j_{z,k}(\xi) \end{aligned} \tag{43}$$

where z is the order of the wavelet scaling functions. $a^j_{z-2,k}$ and $b^j_{z,k}$ are coefficients corresponding to the element nodal axial and bending DOFs in wavelet space, respectively. In general, the order of the scaling function used to approximate the axial displacement will differ from the order approximating the bending DOFs. The selection of the orders of the scaling functions is dependent on the element layout selected in order to ensure that the defined DOFs are positioned at the correct elemental nodes. Therefore, the order of the scaling functions selected to approximate the axial displacement, if the scaling function order approximating the bending DOFs is z, must be $z-2$. Furthermore, the multiresolution scale of the scaling functions is assumed to be of the same scale j. Let the vector $\{\boldsymbol{c_e}\}$ contain the coefficients corresponding to the DOFs within the wavelet-based finite element in wavelet space. Moreover, the vectors ${}^a\left\{\boldsymbol{\Phi}^j_{z-2}(\xi)\right\}$, ${}^t\left\{\boldsymbol{\Phi}^j_z(\xi)\right\}$ and ${}^t\left\{\boldsymbol{\Phi}'^j_z(\xi)\right\}$ contain the scaling functions and the first derivative of the scaling functions approximating the axial deformation, transverse displacements and rotations at the positions corresponding to the related DOFs within the element. Thus, the displacements can be written as:

$$u(\xi) = {}_{(1\times s)}{}^a\left\{\boldsymbol{\Phi}^j_{z-2}(\xi)\right\}_{(s\times 1)}\{\boldsymbol{c_e}\} \tag{44}$$

$$v(\xi) = {}_{(1\times s)}{}^t\left\{\boldsymbol{\Phi}^j_z(\xi)\right\}_{(s\times 1)}\{\boldsymbol{c_e}\} \tag{45}$$

$$\theta(\xi) = \frac{\partial v(\xi)}{\partial x} = \frac{1}{L_e}\frac{\partial v(\xi)}{\partial \xi} = \frac{1}{L_e}{}_{(1\times s)}{}^{t}\left\{\boldsymbol{\Phi}_{z}^{\prime j}(\xi)\right\}_{(s\times 1)}\{\boldsymbol{c_e}\} \tag{46}$$

where

$${}_{(1\times s)}{}^{a}\left\{\boldsymbol{\Phi}_{z-2}^{j}(\xi)\right\} = \left\{\begin{array}{cccccccccc} \phi_{z-2,h}^{j}(\xi) & 0 & 0 & \phi_{z-2,h+1}^{j}(\xi) & 0 & \cdots & 0 & \phi_{z-2,2^j-1}^{j}(\xi) & 0 & 0 \end{array}\right\}$$

$${}_{(1\times s)}{}^{t}\left\{\boldsymbol{\Phi}_{z}^{j}(\xi)\right\} = \left\{\begin{array}{ccccccccc} 0 & \phi_{z,i}^{j}(\xi) & \phi_{z,i+1}^{j}(\xi) & 0 & \cdots & 0 & \phi_{z,2^j-2}^{j}(\xi) & \phi_{z,2^j-1}^{j}(\xi) \end{array}\right\} \tag{47}$$

$${}_{(1\times s)}{}^{t}\left\{\boldsymbol{\Phi}_{z}^{\prime j}(\xi)\right\} = \left\{\begin{array}{ccccccccc} 0 & \phi_{z,i}^{\prime j}(\xi) & \phi_{z,i+1}^{\prime j}(\xi) & 0 & \cdots & 0 & \phi_{z,2^j-2}^{\prime j}(\xi) & \phi_{z,2^j-1}^{\prime j}(\xi) \end{array}\right\}$$

In physical space, the DOFs are expressed as the vector $\{\boldsymbol{h_e}\}$:

$$\{\boldsymbol{h_e}\} = \left\{\begin{array}{cccccccccccc} u_1 & v_1 & \theta_1 & u_2 & v_2 & u_3 & v_3 & \cdots & u_{r-1} & v_{r-1} & u_r & v_r & \theta_r \end{array}\right\}^{T} \tag{48}$$

Therefore, the relation between the physical space and wavelet space DOFs is formulated as:

$${}_{(s\times 1)}\{\boldsymbol{h_e}\} = {}_{(s\times s)}\left[\boldsymbol{R_w}\right]_{(s\times 1)}\{\boldsymbol{c_e}\} \tag{49}$$

The vector containing the coefficients corresponding to the DOFs in wavelet space can be expressed as:

$$\left\{\boldsymbol{c_e}\right\} = \left[\boldsymbol{R_w}\right]^{-1}\left\{\boldsymbol{h_e}\right\} = \left[\boldsymbol{T_w}\right]\left\{\mathbf{h_e}\right\} \tag{50}$$

where the wavelet transformation matrix $\left[\boldsymbol{T_w}\right]$ is the inverse of the matrix $\left[\boldsymbol{R_w}\right]$. The axial deformation, transverse displacement and the rotation DOFs at any elemental node *i* can then be evaluated by substituting Equation (50) into Equations (44)–(46).

$$u(\xi_i) = {}_{(1\times s)}{}^{a}\left\{\boldsymbol{\Phi}_{z}^{j}(\xi_i)\right\}_{(s\times s)}\left[\boldsymbol{T_w}\right]_{(s\times 1)}\{\mathbf{h_e}\} \tag{51}$$

$$v(\xi_i) = {}_{(1\times s)}{}^{t}\left\{\boldsymbol{\Phi}_{z}^{j}(\xi_i)\right\}_{(s\times s)}\left[\boldsymbol{T_w}\right]_{(s\times 1)}\{\mathbf{h_e}\} \tag{52}$$

$$\theta(\xi_i) = \frac{1}{L_e}{}_{(1\times s)}{}^{t}\left\{\boldsymbol{\Phi}_{z}^{\prime j}(\xi)\right\}_{(s\times s)}\left[\boldsymbol{T_w}\right]_{(s\times 1)}\{\mathbf{h_e}\} \tag{53}$$

3.3. The FGM beam wavelet-based finite element formulation

The transverse $v(x)$ and axial $u(x)$ displacements at any point of the beam at time t based on Euler Bernoulli beam theory are expressed as (Şimşek & Kocatürk, 2009):

$$u_0(x,y,t) = u(x,t) - y\frac{\partial v(x,t)}{\partial x} \tag{54}$$

$$v_0(x,y,t) = v(x,t) \tag{55}$$

where x, y and t represent the axial direction, transverse direction and time; u_0 and v_0 are the axial and transverse displacements on the mid-plane of the beam, respectively. This can be expressed in matrix form as:

$$\{d\} = \begin{Bmatrix} u_0 \\ v_0 \end{Bmatrix} = \begin{bmatrix} 1 & 0 & -y \\ 0 & 1 & 0 \end{bmatrix} \begin{Bmatrix} u \\ v \\ \frac{\partial v}{\partial x} \end{Bmatrix} \tag{56}$$

The FGM beam is assumed to undergo small deformations, thus the normal strain in the x direction ε_{xx} can be expressed in terms of the displacement:

$$\varepsilon_{xx} = \frac{\partial u_0}{\partial x} = \frac{\partial u(x,t)}{\partial x} - y\frac{\partial^2 v(x,t)}{\partial x^2} = \begin{bmatrix} 1 & -y \end{bmatrix} \begin{Bmatrix} \frac{\partial u}{\partial x} \\ \frac{\partial^2 v}{\partial x^2} \end{Bmatrix} \tag{57}$$

Since the beam is assumed to be fully elastic, the normal stress in the x direction σ_{xx} is given as:

$$\sigma_{xx} = E(\cdot)\varepsilon_{xx} = E(\cdot)\begin{bmatrix} 1 & -y \end{bmatrix} \begin{Bmatrix} \frac{\partial u}{\partial x} \\ \frac{\partial^2 v}{\partial x^2} \end{Bmatrix} \tag{58}$$

The effective Young's modulus $E(\cdot)$ is based on the power law of material gradation and one can determine the strain energy of the beam element, U_e as (Bathe, 1996):

$$U_e = \frac{1}{2}\int_{vol} \sigma_{xx}^T \varepsilon_{xx} \mathrm{d}V = \frac{1}{2}\iiint_{vol} \sigma_{xx}^T \varepsilon_{xx} \mathrm{d}x\mathrm{d}y\mathrm{d}z \tag{59}$$

Substituting Equations (57) and (58) into Equation (59):

$$U_e = \frac{1}{2}\int_0^b \int_{-\frac{h}{2}}^{\frac{h}{2}} \int_0^1 E(\cdot)\left[\frac{1}{L_e}\left(\frac{\partial u(\xi)}{\partial \xi}\right)^T\left(\frac{\partial u(\xi)}{\partial \xi}\right) - \frac{y}{L_e^2}\left(\frac{\partial^2 v(\xi)}{\partial \xi^2}\right)^T\left(\frac{\partial u(\xi)}{\partial \xi}\right) - \frac{y}{L_e^2}\left(\frac{\partial u(\xi)}{\partial \xi}\right)^T\left(\frac{\partial^2 v(\xi)}{\partial \xi^2}\right) + \frac{y^2}{L_e^3}\left(\frac{\partial^2 v(\xi)}{\partial \xi^2}\right)^T\left(\frac{\partial^2 v(\xi)}{\partial \xi^2}\right)\right]\mathrm{d}\xi\mathrm{d}y\mathrm{d}z \tag{60}$$

The kinetic energy of the wavelet-based FG beam element, Λ_e, is expressed as:

$$\Lambda_e = \iiint_{vol} \rho(\cdot) vel \, \mathrm{d}x \, \mathrm{d}y \, \mathrm{d}z \tag{61}$$

vel is the velocity distribution of the beam. The effective density $\rho(\cdot)$ of the FG beam element is obtained via the power law. The velocity components of the beam in axial and transverse directions can be expressed as:

$$\left(\frac{\partial v_0(x,t)}{\partial t}\right) = \{\dot{v}(x,t)\}$$

$$\left(\frac{\partial u_0(x,y,t)}{\partial t}\right) = \left\{\dot{u}_0(x,y,t)\right\} = \dot{u}(x,t) - y\frac{\partial \dot{v}(x,t)}{\partial x} \tag{62}$$

and using the wavelet scaling functions from Equation (43):

$$\dot{u}(\xi) = {}_{(1\times s)}{}^{a}\left\{\bar{\boldsymbol{\Phi}}_z^j(\xi)\right\}_{(s\times s)}\left[\boldsymbol{T}_p^w\right]_{(s\times 1)}\{\dot{\boldsymbol{h}}^e\} \tag{63}$$

$$\dot{v}(\xi) = {}_{(1\times s)}{}^{t}\left\{\bar{\boldsymbol{\Phi}}_z^j(\xi)\right\}_{(s\times s)}\left[\boldsymbol{T}_p^w\right]_{(s\times 1)}\{\dot{\boldsymbol{h}}^e\} \tag{64}$$

The kinetic energy can now be stated as:

$$\Lambda_e = \frac{1}{2}\int_0^b \int_{-\frac{h}{2}}^{\frac{h}{2}} \int_0^1 \rho(\cdot)\left(L_e(\dot{u}(\xi,t)\dot{u}(\xi,t)) - y\left(\dot{u}(\xi,t)\frac{\partial \dot{v}(\xi,t)}{\partial x}\right) - y\left(\frac{\partial \dot{v}(\xi,t)}{\partial \xi}\dot{u}(\xi,t)\right) + \frac{y^2}{L_e}\left(\frac{\partial \dot{v}(\xi,t)}{\partial x}\frac{\partial \dot{v}(\xi,t)}{\partial x}\right) + L_e(\dot{v}(\xi,t)\dot{v}(\xi,t))\right) \tag{65}$$

3.3.1. Transverse material gradation

Given that the material distribution varies through the thickness of the FG beam, according to the power law the effective Young's modulus $E(y)$and mass density $\rho(y)$ are given as:

$$E(y) = E_{\text{lo}}\left(\left[E_{\text{ratio}} - 1\right]\left(\frac{y}{h} + \frac{1}{2}\right)^n + 1\right) \tag{66}$$

$$\rho(y) = \rho_{\text{lo}}\left(\left[\rho_{\text{ratio}} - 1\right]\left(\frac{y}{h} + \frac{1}{2}\right)^n + 1\right) \tag{67}$$

By substituting Equation (66) into Equation (60), the FG beam potential energy is evaluated as:

$$U_e = \frac{b}{2}\int_{-\frac{h}{2}}^{\frac{h}{2}}\int_0^1 E(y)\left[\frac{1}{L_e}\left(\frac{\partial u(\xi)}{\partial \xi}\right)^T\left(\frac{\partial u(\xi)}{\partial \xi}\right) - \frac{y}{L_e^2}\left(\frac{\partial^2 v(\xi)}{\partial \xi^2}\right)^T\left(\frac{\partial u(\xi)}{\partial \xi}\right) - \frac{y}{L_e^2}\left(\frac{\partial u(\xi)}{\partial \xi}\right)^T\left(\frac{\partial^2 v(\xi)}{\partial \xi^2}\right) + \frac{y^2}{L_e^3}\left(\frac{\partial^2 v(\xi)}{\partial \xi^2}\right)^T\left(\frac{\partial^2 v(\xi)}{\partial \xi^2}\right)\right]\mathrm{d}\xi\mathrm{d}y \tag{68}$$

Let

$${}^{A}E_e = \int_{-\frac{h}{2}}^{\frac{h}{2}} E(y)\mathrm{d}y = \int_{-\frac{h}{2}}^{\frac{h}{2}}\left(E_{\mathrm{lo}}\left(\left[E_{\mathrm{ratio}}-1\right]\left(\frac{y}{h}+\frac{1}{2}\right)^n+1\right)\right)\mathrm{d}y \tag{69}$$

$${}^{B}E_e = \int_{-\frac{h}{2}}^{\frac{h}{2}} yE(y)\mathrm{d}y = \int_{-\frac{h}{2}}^{\frac{h}{2}}\left(yE_{\mathrm{lo}}\left(\left[E_{\mathrm{ratio}}-1\right]\left(\frac{y}{h}+\frac{1}{2}\right)^n+1\right)\right)\mathrm{d}y \tag{70}$$

$${}^{C}E_e = \int_{-\frac{h}{2}}^{\frac{h}{2}} y^2E(y)\mathrm{d}y = \int_{-\frac{h}{2}}^{\frac{h}{2}}\left(y^2E_{\mathrm{lo}}\left(\left[E_{\mathrm{ratio}}-1\right]\left(\frac{y}{h}+\frac{1}{2}\right)^n+1\right)\right)\mathrm{d}y \tag{71}$$

where ${}^{A}E_e$, ${}^{B}E_e$ and ${}^{C}E_e$ denote the axial, axial-bending coupling and bending stiffness of the wavelet-based finite element, respectively. The wavelet space axial stiffness matrix ${}^{A,1}[\boldsymbol{k}_e^{\boldsymbol{w}}]$ of the WFE is evaluated by substituting Equation (43) into Equation (68).

$${}^{A,1}_{(s\times s)}[\boldsymbol{k}_e^{\boldsymbol{w}}] = \int_0^1 a\left\{\frac{\partial \boldsymbol{\Phi}^j_{z-2}(\xi)}{\partial \xi}\right\}^T a\left\{\frac{\partial \boldsymbol{\Phi}^j_{z-2}(\xi)}{\partial \xi}\right\}\mathrm{d}\xi \tag{72}$$

The axial-bending coupling stiffness matrices ${}^{B,1}[\boldsymbol{k}_e^{\boldsymbol{w}}]$ and ${}^{C,1}[\boldsymbol{k}_e^{\boldsymbol{w}}]$ in wavelet space are given as:

$${}^{B,1}_{(s\times s)}[\boldsymbol{k}_e^{\boldsymbol{w}}] = \int_0^1 t\left\{\frac{\partial^2 \boldsymbol{\Phi}^j_{z}(\xi)}{\partial \xi^2}\right\}^T a\left\{\frac{\partial \boldsymbol{\Phi}^j_{z-2}(\xi)}{\partial \xi}\right\}\mathrm{d}\xi \tag{73}$$

$${}^{C,1}_{(s\times s)}[\boldsymbol{k}_e^{\boldsymbol{w}}] = \int_0^1 a\left\{\frac{\partial \boldsymbol{\Phi}^j_{z-bf2}(\xi)}{\partial \xi}\right\}^T t\left\{\frac{\partial^2 \boldsymbol{\Phi}^j_{z}(\xi)}{\partial \xi^2}\right\}\mathrm{d}\xi \tag{74}$$

The wavelet space bending stiffness matrix ${}^{D,1}[\boldsymbol{k}_e^{\boldsymbol{w}}]$ is:

$$ {}^{D,1}_{(s\times s)}[\boldsymbol{k}_e^{w}] = \int_0^1 {}^{t}\left\{\frac{\partial^2 \boldsymbol{\Phi}_z^{j}(\xi)}{\partial \xi^2}\right\}^{T} {}^{t}\left\{\frac{\partial^2 \boldsymbol{\Phi}_z^{j}(\xi)}{\partial \xi^2}\right\} \mathrm{d}\xi \tag{75} $$

The matrices in Equations (72)–(75) are transformed into the physical space via the transformation matrix $[\boldsymbol{T}_w]$. Thus, in physical space the stiffness matrices are evaluated as:

$$ {}^{A,1}_{(s\times s)}[\boldsymbol{k}_e^{p}] = \frac{b^A E_e}{L_e}[\boldsymbol{T}_w]^{T} {}^{A,1}[\boldsymbol{k}_e^{w}][\boldsymbol{T}_w] \tag{76} $$

$$ {}^{B,1}_{(s\times s)}[\boldsymbol{k}_e^{p}] = \frac{b^B E_e}{L_e^2}[\boldsymbol{T}_w]^{T} {}^{B,1}[\boldsymbol{k}_e^{w}][\boldsymbol{T}_w] \tag{77} $$

$$ {}^{C,1}_{(s\times s)}[\boldsymbol{k}_e^{p}] = \frac{b^B E_e}{L_e^2}[\boldsymbol{T}_w]^{T} {}^{C,1}[\boldsymbol{k}_e^{w}][\boldsymbol{T}_w] \tag{78} $$

$$ {}^{D,1}_{(s\times s)}[\boldsymbol{k}_e^{p}] = \frac{b^C E_e}{L_e^3}[\boldsymbol{T}_w]^{T} {}^{D,1}[\boldsymbol{k}_e^{w}][\boldsymbol{T}_w] \tag{79} $$

The FGM beam element stiffness matrix in physical space is obtained as:

$$ {}_{(s\times s)}{}^{1}[\boldsymbol{k}_e^{p}] = {}^{A,1}[\boldsymbol{k}_e^{p}] - {}^{B,1}[\boldsymbol{k}_e^{p}] - {}^{C,1}[\boldsymbol{k}_e^{p}] + {}^{D,1}[\boldsymbol{k}_e^{p}] \tag{80} $$

Similarly, the kinetic energy of the FG beam as the material distribution varies through the thickness of the beam is evaluated when Equation (67) is substituted into Equation (65).

$$ \Lambda_e = \frac{b}{2}\int_{-\frac{h}{2}}^{\frac{h}{2}}\int_0^1 \rho(y)\left(L_e(\dot{u}(\xi,t)\dot{u}(\xi,t)) - y\left(\dot{u}(\xi,t)\frac{\partial \dot{v}(\xi,t)}{\partial x}\right) - y\left(\frac{\partial \dot{v}(\xi,t)}{\partial \xi}\dot{u}(\xi,t)\right) + \frac{y^2}{L_e}\left(\frac{\partial \dot{v}(\xi,t)}{\partial x}\frac{\partial \dot{v}(\xi,t)}{\partial x}\right) + L_e(\dot{v}(\xi,t)\dot{v}(\xi,t))\right)\mathrm{d}\xi\mathrm{d}y \tag{81} $$

Let the inertial coefficients be denoted as:

$$ {}^{A}\rho_e = \int_{-\frac{h}{2}}^{\frac{h}{2}} \rho(y)\mathrm{d}y = \int_{-\frac{h}{2}}^{\frac{h}{2}} \rho_{\mathrm{lo}}\left(\left[\rho_{\mathrm{ratio}} - 1\right]\left(\frac{y}{h} + \frac{1}{2}\right)^{n} + 1\right)\mathrm{d}y \tag{82} $$

$$ {}^{B}\rho_e = \int_{-\frac{h}{2}}^{\frac{h}{2}} y\rho(y)\mathrm{d}y = \int_{-\frac{h}{2}}^{\frac{h}{2}} \left(y\rho_{\mathrm{lo}}\left(\left[\rho_{\mathrm{ratio}} - 1\right]\left(\frac{y}{h} + \frac{1}{2}\right)^{n} + 1 \right)\right)\mathrm{d}y \tag{83} $$

$$ {}^{C}\rho_e = \int_{-\frac{h}{2}}^{\frac{h}{2}} y^2\rho(y)\mathrm{d}y = \int_{-\frac{h}{2}}^{\frac{h}{2}} \left(y^2\rho_{\mathrm{lo}}\left(\left[\rho_{\mathrm{ratio}} - 1\right]\left(\frac{y}{h} + \frac{1}{2}\right)^{n} + 1 \right)\right)\mathrm{d}y \tag{84} $$

Substituting Equations (63) and (64) into (81), the mass matrix components in wavelet space are evaluated as follows:

$$ {}^{A,1}_{(s\times s)}[\boldsymbol{m}_e^{w}] = \int_0^1 {}^{a}\left\{ \boldsymbol{\Phi}^{j}_{z-2}(\xi) \right\}^{T} {}^{a}\left\{ \boldsymbol{\Phi}^{j}_{z-2}(\xi) \right\}\mathrm{d}\xi \tag{85} $$

$$ {}^{B,1}_{(s\times s)}[\boldsymbol{m}_e^{w}] = \int_0^1 {}^{a}\left\{ \boldsymbol{\Phi}^{j}_{z-2}(\xi) \right\}^{T} {}^{t}\left\{ \frac{\partial \boldsymbol{\Phi}^{j}_{z}(\xi)}{\partial \xi} \right\}\mathrm{d}\xi \tag{86} $$

$$ {}^{C,1}_{(s\times s)}[\boldsymbol{m}_e^{w}] = \int_0^1 {}^{t}\left\{ \frac{\partial \boldsymbol{\Phi}^{j}_{z}(\xi)}{\partial \xi} \right\}^{T} {}^{a}\left\{ \boldsymbol{\Phi}^{j}_{z-2}(\xi) \right\}\mathrm{d}\xi \tag{87} $$

$$ {}^{D,1}_{(s\times s)}[\boldsymbol{m}_e^{w}] = \int_0^1 {}^{t}\left\{ \frac{\partial \boldsymbol{\Phi}^{j}_{z}(\xi)}{\partial \xi} \right\}^{T} {}^{t}\left\{ \frac{\partial \boldsymbol{\Phi}^{j}_{z}(\xi)}{\partial \xi} \right\}\mathrm{d}\xi \tag{88} $$

$$ {}^{E,1}_{(s\times s)}[\boldsymbol{m}_e^{w}] = \int_0^1 {}^{t}\left\{ \boldsymbol{\Phi}^{j}_{z}(\xi) \right\}^{T} {}^{t}\left\{ \boldsymbol{\Phi}^{j}_{z}(\xi) \right\}\mathrm{d}\xi \tag{89} $$

The mass matrices in the physical space, after transformation via the wavelet transformation matrix $[\boldsymbol{T}_w]$, can be written as:

$$ {}^{A,1}_{(s\times s)}[\boldsymbol{m}_e^{p}] = b^{A}\rho_e L_e \left[\boldsymbol{T}_w\right]^{T} {}^{A,1}[\boldsymbol{m}_e^{w}]\left[\boldsymbol{T}_w\right] \tag{90} $$

$$ {}^{B,1}_{(s\times s)}[\boldsymbol{m}_e^{p}] = b^{B}\rho_e \left[\boldsymbol{T}_w\right]^{T} {}^{B,1}[\boldsymbol{m}_e^{w}]\left[\boldsymbol{T}_w\right] \tag{91} $$

$$ {}^{C,1}_{(s\times s)}[\boldsymbol{m}_e^{p}] = b^{B}\rho_e \left[\boldsymbol{T}_w\right]^{T} {}^{C,1}[\boldsymbol{m}_e^{w}]\left[\boldsymbol{T}_w\right] \tag{92} $$

$$ {}^{D,1}_{(s\times s)}[\boldsymbol{m}_e^p] = \frac{b^C \rho_e}{L_e}\left[\boldsymbol{T}_w\right]^T {}^{D,1}[\boldsymbol{m}_e^w]\left[\boldsymbol{T}_w\right] \tag{93} $$

$$ {}^{E,1}_{(s\times s)}[\boldsymbol{m}_e^p] = b^A \rho_e L_e \left[\boldsymbol{T}_w\right]^T {}^{E,1}[\boldsymbol{m}_e^w]\left[\boldsymbol{T}_w\right] \tag{94} $$

The total element mass matrix in physical space for the wavelet-based FGM beam is obtained as:

$$ {}_{(s\times s)}{}^{1}[\boldsymbol{m}_e^p] = {}^{A,1}[\boldsymbol{m}_e^p] - {}^{B,1}[\boldsymbol{m}_e^p] - {}^{C,1}[\boldsymbol{m}_e^p] + {}^{D,1}[\boldsymbol{m}_e^p] + {}^{E,1}[\boldsymbol{m}_e^p] \tag{95} $$

3.3.2. Axial material gradation

In this case, the material distribution is assumed to vary along the length of the FG beam according to the power law and the effective Young's modulus $E(x)$and mass density $\rho(x)$ of the beam are given as:

$$ E(\xi) = E_r\left(\left[E_{\text{ratio}} - 1\right](1-\xi)^n + 1\right) \tag{96} $$

$$ \rho(\xi) = \rho_r\left(\left[\rho_{\text{ratio}} - 1\right](1-\xi)^n + 1\right) \tag{97} $$

By substituting Equation (96) into Equation (60), the FG beam potential energy is evaluated as:

$$ U_e = \frac{1}{2}\int_0^b \int_{-\frac{h}{2}}^{\frac{h}{2}} \int_0^1 E(\xi)\left[\frac{1}{L_e}\left(\frac{\partial u(\xi)}{\partial \xi}\right)^T\left(\frac{\partial u(\xi)}{\partial \xi}\right) - \frac{y}{L_e^2}\left(\frac{\partial^2 v(\xi)}{\partial \xi^2}\right)^T\left(\frac{\partial u(\xi)}{\partial \xi}\right) - \frac{y}{L_e^2}\left(\frac{\partial u(\xi)}{\partial \xi}\right)^T\left(\frac{\partial^2 v(\xi)}{\partial \xi^2}\right) + \frac{y^2}{L_e^3}\left(\frac{\partial^2 v(\xi)}{\partial \xi^2}\right)^T\left(\frac{\partial^2 v(\xi)}{\partial \xi^2}\right)\right] \mathrm{d}\xi \mathrm{d}y \mathrm{d}z \tag{98} $$

However, given that the properties of the material are uniform through the cross section of the FG beam, then

$$ \int_0^b \int_{-\frac{h}{2}}^{\frac{h}{2}} \mathrm{d}y\mathrm{d}z = A, \int_0^b \int_{-\frac{h}{2}}^{\frac{h}{2}} y\mathrm{d}y\mathrm{d}z = 0 \text{ and } \int_0^b \int_{-\frac{h}{2}}^{\frac{h}{2}} y^2 \mathrm{d}y\mathrm{d}z = I \tag{99} $$

where A is the cross-sectional area of the beam and I is the moment of inertia. Therefore, Equation (98) can be expressed as:

$$ U_e = \frac{1}{2}\int_0^1 E(\xi)\left[\frac{A}{L_e}\left(\frac{\partial u(\xi)}{\partial \xi}\right)^T\left(\frac{\partial u(\xi)}{\partial \xi}\right) + \frac{I}{L_e^3}\left(\frac{\partial^2 v(\xi)}{\partial \xi^2}\right)^T\left(\frac{\partial^2 v(\xi)}{\partial \xi^2}\right)\right] \mathrm{d}\xi \tag{100} $$

The wavelet space axial stiffness matrix ${}^{A,2}[\boldsymbol{k}_e^w]$ of the WFE is evaluated by substituting Equation (43) into Equation (100).

$$ {}^{A,2}_{(s\times s)}[\boldsymbol{k}_e^w] = \int_0^1 E(\xi)^a \left\{ \frac{\partial \boldsymbol{\Phi}^j_{z-2}(\xi)}{\partial \xi} \right\}^T {}_a \left\{ \frac{\partial \boldsymbol{\Phi}^j_{z-2}(\xi)}{\partial \xi} \right\} \mathrm{d}\xi \tag{101} $$

The wavelet space bending stiffness matrix ${}^{B,2}[\boldsymbol{k}_e^w]$ is:

$$ {}^{B,2}_{(s\times s)}[\boldsymbol{k}_e^w] = \int_0^1 E(\xi)^t \left\{ \frac{\partial^2 \boldsymbol{\Phi}^j_z(\xi)}{\partial \xi^2} \right\}^T {}_t \left\{ \frac{\partial^2 \boldsymbol{\Phi}^j_z(\xi)}{\partial \xi^2} \right\} \mathrm{d}\xi \tag{102} $$

The stiffness matrices in physical space are obtained by applying the wavelet transformation matrix $\left[\boldsymbol{T}_w\right]$ to Equations (101) and (102) and are obtained as:

$$ {}^{A,2}_{(s\times s)}[\boldsymbol{k}_e^p] = \frac{A}{L_e}\left[\boldsymbol{T}_w\right]^T {}^{A,2}[\boldsymbol{k}_e^w]\left[\boldsymbol{T}_w\right] \tag{103} $$

$$ {}^{B,2}_{(s\times s)}[\boldsymbol{k}_e^p] = \frac{I}{L_e^3}\left[\boldsymbol{T}_w\right]^T {}^{B,2}[\boldsymbol{k}_e^w]\left[\boldsymbol{T}_w\right] \tag{104} $$

The axial varying FGM beam element stiffness matrix in physical space is obtained as:

$$ {}^{2}_{(s\times s)}[\boldsymbol{k}_e^p] = {}^{A,2}[\boldsymbol{k}_e^p] + {}^{B,2}[\boldsymbol{k}_e^p] \tag{105} $$

The kinetic energy of the axially varying FG beam is evaluated when Equations (97) and (99) are substituted into Equation (65).

$$ \Lambda_e = \frac{1}{2}\int_0^1 \rho(\xi)\left(AL_e(\dot{u}(\xi,t)\dot{u}(\xi,t)) + \frac{I}{L_e}\left(\frac{\partial \dot{v}(\xi,t)}{\partial x}\frac{\partial \dot{v}(\xi,t)}{\partial x} \right) + AL_e(\dot{v}(\xi,t)\dot{v}(\xi,t)) \right)\mathrm{d}\xi\mathrm{d}y\mathrm{d}z \tag{106} $$

Thus, the component mass matrices in wavelet space are obtained as:

$$ {}^{A,2}_{(s\times s)}[\boldsymbol{m}_e^w] = \int_0^1 \rho(\xi)^a \left\{ \boldsymbol{\Phi}^j_{z-2}(\xi) \right\}^T {}_a \left\{ \boldsymbol{\Phi}^j_{z-2}(\xi) \right\} \mathrm{d}\xi \tag{107} $$

$$ {}^{B,2}_{(s\times s)}[\boldsymbol{m}_e^w] = \int_0^1 \rho(\xi)^t \left\{ \frac{\partial \boldsymbol{\Phi}^j_z(\xi)}{\partial \xi} \right\}^T {}_t \left\{ \frac{\partial \boldsymbol{\Phi}^j_z(\xi)}{\partial \xi} \right\} \mathrm{d}\xi \tag{108} $$

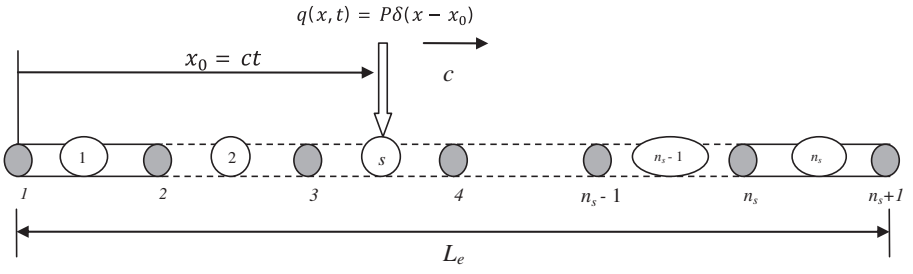

Figure 8. Layout of a beam WFE subjected to a moving point load.

$$ {}^{C,2}_{(s\times s)}[\boldsymbol{m}_e^w] = \int_0^1 \rho(\xi)^t \left\{ \boldsymbol{\Phi}_z^j(\xi) \right\}^T {}^t \left\{ \boldsymbol{\Phi}_z^j(\xi) \right\} \mathrm{d}\xi \tag{109} $$

The mass matrices in the physical space, after transformation via the wavelet transformation matrix $[\boldsymbol{T}_w]$, can be written as:

$$ {}^{A,2}_{(s\times s)}[\boldsymbol{m}_e^p] = AL_e [\boldsymbol{T}_w]^T {}^{A,2}[\boldsymbol{m}_e^w][\boldsymbol{T}_w] \tag{110} $$

$$ {}^{B,2}_{(s\times s)}[\boldsymbol{m}_e^p] = \frac{I}{L_e} [\boldsymbol{T}_w]^T {}^{B,2}[\boldsymbol{m}_e^w][\boldsymbol{T}_w] \tag{111} $$

$$ {}^{C,2}_{(s\times s)}[\boldsymbol{m}_e^p] = AL_e [\boldsymbol{T}_w]^T {}^{C,2}[\boldsymbol{m}_e^w][\boldsymbol{T}_w] \tag{112} $$

The total element mass matrix in physical space for the wavelet-based FG beam is obtained as:

$$ {}^{2}_{(s\times s)}[\boldsymbol{m}_e^p] = {}^{A,2}[\boldsymbol{m}_e^p] + {}^{B,2}[\boldsymbol{m}_e^p] + {}^{C,2}[\boldsymbol{m}_e^p] \tag{113} $$

4. Wavelet-based moving load vector

Moving load problems are often characterised by the loading conditions varying in location and/or magnitude with respect to time. Taking into consideration a simply supported beam subjected to a moving load represented by the function $q(x,t) = P\delta(x - x_0)$ where P is the magnitude of the moving point load, $\delta(x)$ is the Dirac Delta function and x_0 is the distance travelled by the moving load at time t from the left edge of the beam. In order to demonstrate the evaluation of the wavelet-based moving load vectors, consider a moving point load travelling across a wavelet finite beam element as illustrated in Figure 8.

Assuming the beam is modelled using one wavelet-based finite element, the moving load travelling at a constant speed of c m s^{-1} is expressed as (Fryba, 1999):

$$ q(x,t) = P\delta(x - x_0) \tag{114} $$

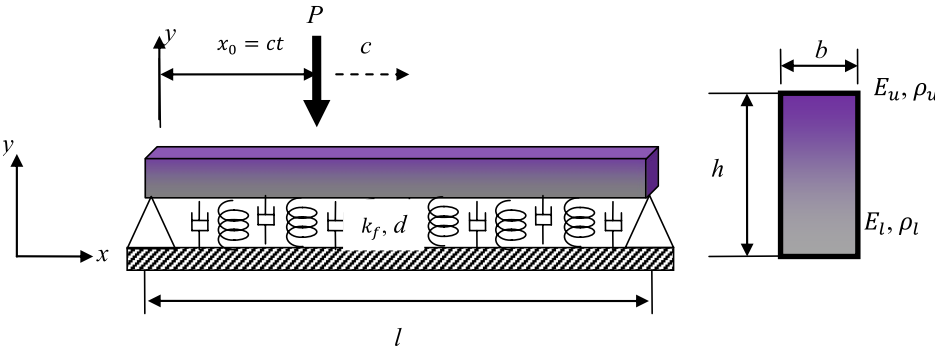

Figure 9. Simply supported FG beam resting on a viscoelastic foundation subjected to a moving load point load.

where $x_0 = ct$ is the distance travelled by the load at time t. The position of the moving load in natural coordinates within the WFE at time t s is $\xi_0 = \frac{x_0}{L_e}$. At a given time t, the moving load is at position ξ_0 and the potential work of the load at that instant is therefore expressed as:

$$\Omega_e^b(\xi_0) = \int_0^1 P\delta(\xi - \xi_0)v(\xi)\mathrm{d}\xi = P\{\boldsymbol{v}_e\}^T \left[\boldsymbol{T}_w\right]^{T_t} \left\{\boldsymbol{\Phi}_z^j(\xi_0)\right\}^T \tag{115}$$

Therefore, the element load vector in wavelet space is obtained from Equation (115) as:

$$_{(s\times 1)}\left\{\boldsymbol{f}_e^w(t)\right\} = {}^t\left\{\boldsymbol{\Phi}_z^j(\xi_0)\right\}^T \tag{116}$$

and subsequently in physical space

$$_{(s\times 1)}\left\{\boldsymbol{f}_e^p(t)\right\} = \begin{Bmatrix} 0 \\ f_{y1} \\ \acute{m}_1 \\ 0 \\ f_{y2} \\ 0 \\ \vdots \\ f_{yr-1} \\ 0 \\ f_{yr} \\ \acute{m}_r \end{Bmatrix} = P\left[\boldsymbol{T}_w\right]^{T_t} \left\{\boldsymbol{\Phi}_z^j(\xi_0)\right\}^T \tag{117}$$

Table 1. The non-dimensional fundamental frequency of a simply supported FGM beam for varying composition distributions and $\boldsymbol{E}_{\text{ratio}}$.($\frac{\rho_u}{\rho_l} = 1$, $\frac{l}{h} = 20$).

E_{ratio}		$n=0$	$n=.1$	$n=.2$	$n=1$	$n=2$	$n=10$	$n=10^4$
.25	Ref.	2.2203	2.3739	2.4606	2.7035	2.8053	3.0084	–
	FEM	2.2203	2.37469	2.46153	2.70437	2.80598	3.00855	3.13981
	$D12_0$	2.2203	2.37459	2.46113	2.7039	2.80562	3.0085	3.1398
	$BSWI5_4$	2.2203	2.37459	2.46113	2.7039	2.80562	3.0085	3.1398
.5	Ref.	2.6403	2.7104	2.7573	2.8944	2.9459	3.0562	–
	FEM	2.6404	2.71075	2.75767	2.89474	2.94622	3.05632	3.13987
	$D12_0$	2.6404	2.71073	2.75762	2.89459	2.94609	3.05629	3.13986
	$BSWI5_4$	2.6404	2.71073	2.75762	2.89459	2.94609	3.05629	3.13986
1	Ref.	3.1399	3.1399	3.1399	3.1399	3.1399	3.1399	3.1399
	FEM	3.13998	3.13998	3.13998	3.13998	3.13998	3.13998	3.13998
	$D12_0$	3.13998	3.13998	3.13998	3.13998	3.13998	3.13998	3.13998
	$BSWI5_4$	3.13998	3.13998	3.13998	3.13998	3.13998	3.13998	3.13998
2	Ref.	3.734	3.6775	3.6301	3.4421	3.3765	3.2725	–
	FEM	3.73409	3.67727	3.62998	3.44245	3.3769	3.27269	3.14022
	$D12_0$	3.73409	3.67726	3.62994	3.44226	3.37668	3.27262	3.14022
	$BSWI5_4$	3.73409	3.67726	3.62994	3.44226	3.37668	3.27262	3.14022
4	Ref.	4.4406	4.337	4.2459	3.8234	3.6485	3.4543	–
	FEM	4.44061	4.33664	4.24558	3.82455	3.65012	3.45511	3.14069
	$D12_0$	4.4406	4.33661	4.2455	3.82389	3.64923	3.45473	3.14069
	$BSWI5_4$	4.4406	4.33661	4.2455	3.82489	3.64923	3.45473	3.14069

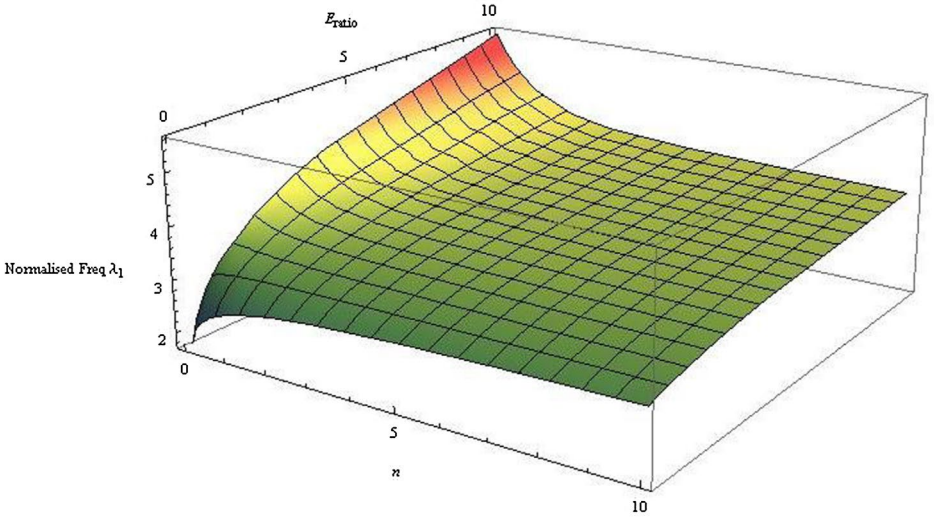

Figure 10. 3D plot of the non-dimensional fundamental frequency variation with respect to E_{ratio} and n for $l/h = 20$ using the $BSWI5_4$ WFEM.

Table 2. Material properties of FG beam constituent materials.

Properties	Steel	Alunima (Al_2O_3)	Units
E	2.1×10^{11}	3.9×10^{11}	Pa
ρ	7.8×10^{3}	3.96×10^{3}	kg m^{-3}

The vector $\left\{\boldsymbol{f}_e^p(t)\right\}$ contains the equivalent WFE nodal forces and moments vector of the moving load, acting on element e in physical space, corresponding to the

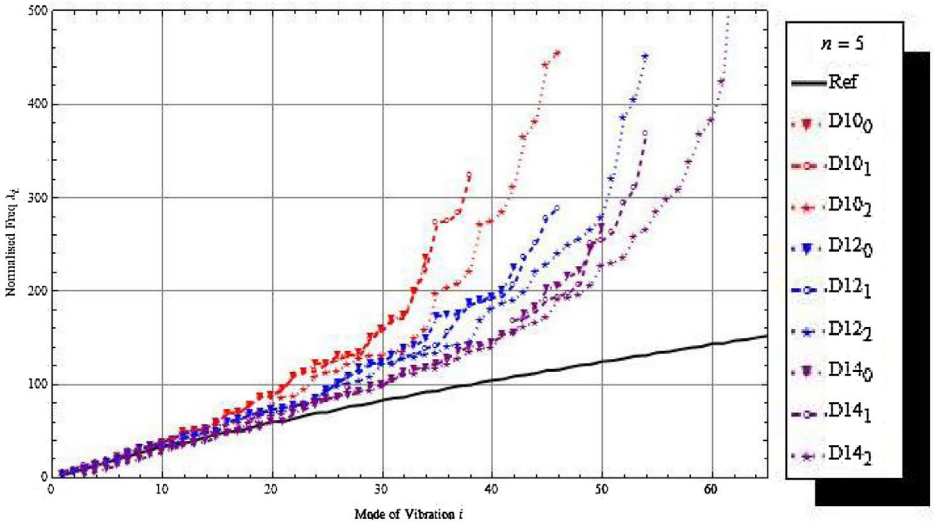

Figure 11. The comparison of the non-dimensional frequencies using the different orders and scales of the DL_j WFE for $n = 5$, and $l/h = 100$.

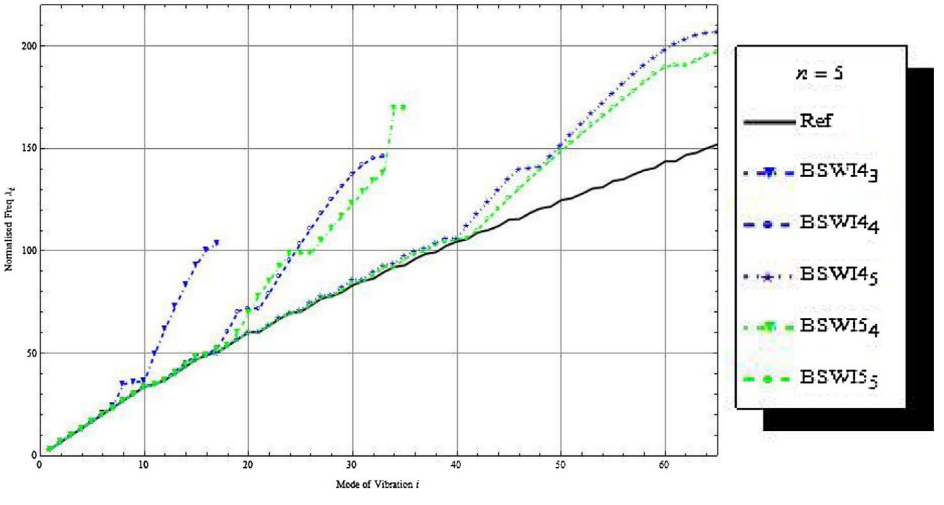

Figure 12. The comparison of the non-dimensional frequencies using the different orders and scales of the BSWIm_j WFE for $n = 5$, and $l/h = 100$.

transverse moving load position ξ_0 at time t; as illustrated in Figure 8. Given that the location and/or magnitude of the load varies with time and assuming at a new time the moving load is still acting within the same WFE; the new load vector is obtained via the scaling functions in Equation (43) with respect to the new location of the moving load in natural coordinates i.e. the new value of position ξ_0. The numerical values of the shape functions and consequently the load vector in wavelet space will change according to this new external force location. Subsequently,

the load vector in physical space, corresponding to the new location with respect to time, is evaluated by implementing the wavelet transformation matrix to the new wavelet space load vector. The other WFEs within the system that have no action of an external load at a particular time t have zero entries within the load vectors. When the moving load is acting on a new WFE, the scaling functions corresponding to the WFE subjected to the moving load are used to obtain the load vector for that particular element. Hence, as the moving load travels from one WFE to the next, there is a shift in position of the equivalent WFE load vector with non-zero entries.

5. Numerical examples

Several numerical results are presented in this section to validate and highlight some key features of the wavelet-based FG beam element approach for dynamic analysis of FG beams. An initial free vibration analysis is carried out and compared with results presented in (Şimşek & Kocatürk, 2009). Furthermore, the analysis of a FG beam resting on a viscoelastic foundation is presented to investigate the effect of the material distribution, the moving load velocity and damping on the dynamic response of the system. The Daubechies and BSWI WFEMs are compared with the classical FEM and in some cases previously published works.

5.1. Free vibration analysis

Preliminary results in this section are obtained for the free vibration analysis of a simply supported FG beam. The FG beam of length l and uniform cross-sectional area A (width $b = .4$ m and height $h = .9$ m), has a Young's modulus E_u, E_l and material density ρ_u, ρ_l at the upper and lower surfaces, respectively; as illustrated in Figure 9. In this analysis, the upper surface material is alumina of Young's modulus $E_u = 390$ GPa and density $\rho_u = 3960$ kg m^{-3}. The density ratio of the two surfaces is assumed to be equal to one i.e. $\rho_{\text{ratio}} = \frac{\rho_u}{\rho_l} = 1$. Given that $E_{\text{ratio}} = \frac{E_u}{E_l}$, the Young's modulus of the lower surface is evaluated from the relation $E_l = \frac{E_u}{E_{\text{ratio}}}$.

The effective material properties are evaluated for different material distributions from Equation (41) by altering the value of n. The free vibration analysis is carried out by solving the eigenvalue problem:

$$[[\boldsymbol{K}] - \omega^2[\boldsymbol{M}]]\{\acute{\boldsymbol{U}}\} = 0 \tag{118}$$

where the matrices $[\boldsymbol{M}]$ and $[\boldsymbol{K}]$ are the mass and stiffness matrices of the system in physical space, respectively. They are computed by assembling the elemental stiffness and mass matrices in Equations (80) and (95), respectively, and then applying the boundary conditions. The vector $\left\{\acute{\boldsymbol{U}}\right\}$ represents modal displacements and ω is the corresponding natural frequencies of the system. The non-dimensional frequencies λ_i of the FG beam are evaluated from the relation:

$$\lambda_i^2 = \omega_i l^2 \left(\frac{12\rho_l}{E_l h^2} \right)^{\frac{1}{2}} \tag{119}$$

where ω_i is the ith mode natural frequency of the beam in rad s^{-1}.

The implementation of the wavelet-based FG beam element approach is validated by comparing the fundamental frequencies, for variations in material distribution and E_{ratio} for beam slenderness ratio $l/h = 20$, with results presented by Simsek and Kocaturk (indicated by "Ref.") (Şimşek & Kocatürk, 2009) as shown in Table 1.

Two Daubechies WFEs for wavelet family order $L = 12$ and scale $j = 0$ ($D12_0$) are compared with the BSWI WFEM solution obtained using one WFE of wavelet family order $m = 5$ at scale $j = 4$ ($BSWI5_4$). The selection of the number of elements implemented, order and multiresolution scale of the wavelet-based elements, allow for a comparison of the results with a similar number of DOFs (37 and 38 DOFs, respectively) within the entire FG beam. Furthermore, the results are compared with the classical FEM solution, where 12 elements (39 DOFs) are implemented.

It is observed that the results obtained via both WFEM solutions are in excellent agreement with those presented by (Şimşek & Kocatürk, 2009) hence validating the use of the method in the free vibration analysis of FG beams. Furthermore, the results are relatively more accurate when compared with the FEM solution with fewer elements used to model the system.

Moreover, increasing the value of E_{ratio} leads to an increase in the non-dimensional fundamental frequency for a particular material distribution. When $E_{\text{ratio}} < 1$, it is observed that as n increases, the fundamental frequency also increases. This is because the lower surface material has a higher bending rigidity than the top alumina surface and increasing the value of n leads to an increase of the effective Young's modulus and consequently bending stiffness of the FG beam. However, when $E_{\text{ratio}} > 1$, increasing n results in a decrease of the non-dimensional fundamental frequency since $E_l < E_u$. For $E_{\text{ratio}} = 1$, the FG beam is fully homogenous and the variation of the power law exponent n does not affect the material distribution. Thus, the non-dimensional fundamental frequency remains constant for all values of n. These observations are further made from the graphical representation of the results presented in Figure 10. Notably, for a large value of n, the effect of E_{ratio} on the non-dimensional frequencies is not as significant as when n is small. Therefore, decreasing the value of n increases the effectiveness of E_{ratio} on the non-dimensional frequencies. The higher non-dimensional frequencies follow the same trend and these highlighted observations are consistent with the findings presented in (Alshorbagy et al., 2011; Şimşek & Kocatürk, 2009).

In the second part of the free vibration analysis of a simply supported FG beam, the effects of altering the wavelet family order and/or multiresolution scale is investigated and the performance of the BSWI and Daubechies WFEM solutions

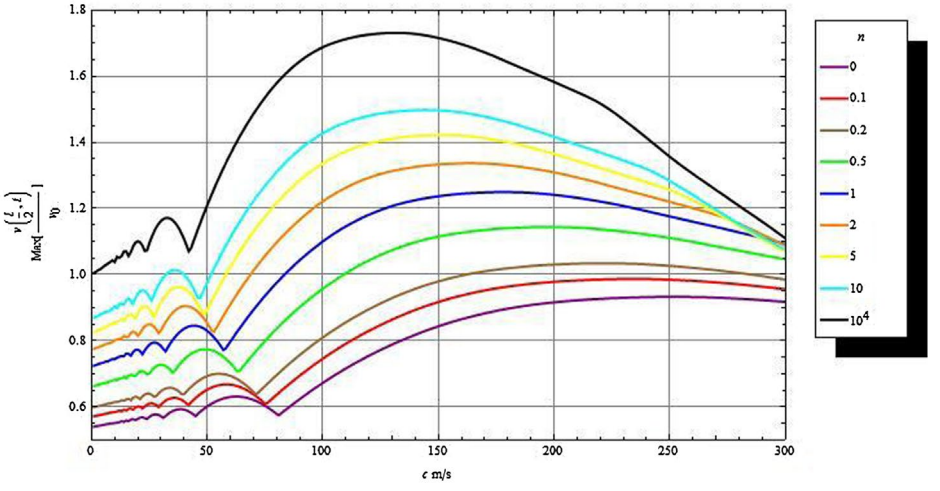

Figure 13. Variation of the maximum non-dimensional vertical displacement at the centre of a simply supported FG beam subjected to a moving load with respect to the load velocities for different *n*.

Table 3. The critical velocity and maximum normalised deflection at the centre of a transversely varying steel-alumina FG beam for different values of ***n***.

	Critical velocity c m s^{-1}				$\text{Max}\left[\frac{v\left(\frac{l}{2},t\right)}{v_0}\right]$			
n	Ref.	FEM	$D12_0$	$BSWI4_3$	Ref.	FEM	$D12_0$	$BSWI4_3$
0	252	252	252	252	.9328	.9322	.9323	.9322
.1	–	235	235	235	–	.9863	.9864	.9863
.2	222	222	222	222	1.0344	1.0340	1.0340	1.0340
.5	198	198	198	198	1.1444	1.1435	1.1437	1.1436
1	179	178	178	178	1.2503	1.2491	1.2495	1.2493
2	164	164	164	164	1.3376	1.3363	1.3368	1.3365
3	–	157	158	158	–	1.3747	1.3751	1.3748
5	–	151	151	152	–	1.4217	1.422	1.4218
7	–	148	148	148	–	1.4567	1.4570	1.4568
10	–	145	145	145	–	1.4974	1.4976	1.4974
10^4	132	132	132	132	–	1.7308	1.7309	1.7308

compared. A steel-alumina FG beam is analysed and the material properties of the constituent materials presented in Table 2.

In the analysis, the top surface is alumina and the bottom surface is steel. The beam is approximated to be a homogeneous steel beam when the power law exponent $n = 10^4$ and is fully alumina when $n = 0$. The 2 element $BSWI5_5$ (137 DOFs) WFEM solution for the non-dimensional frequencies converge and are used as a reference for the comparison of the performance of the different solutions.

The Daubechies scaling functions have no closed form solution hence numerical errors arise when evaluating the connection coefficients, as described in Section 2.2, which are used to formulate the elemental matrices. However, the accuracy of the results can be improved by increasing the order and/or multiresolution

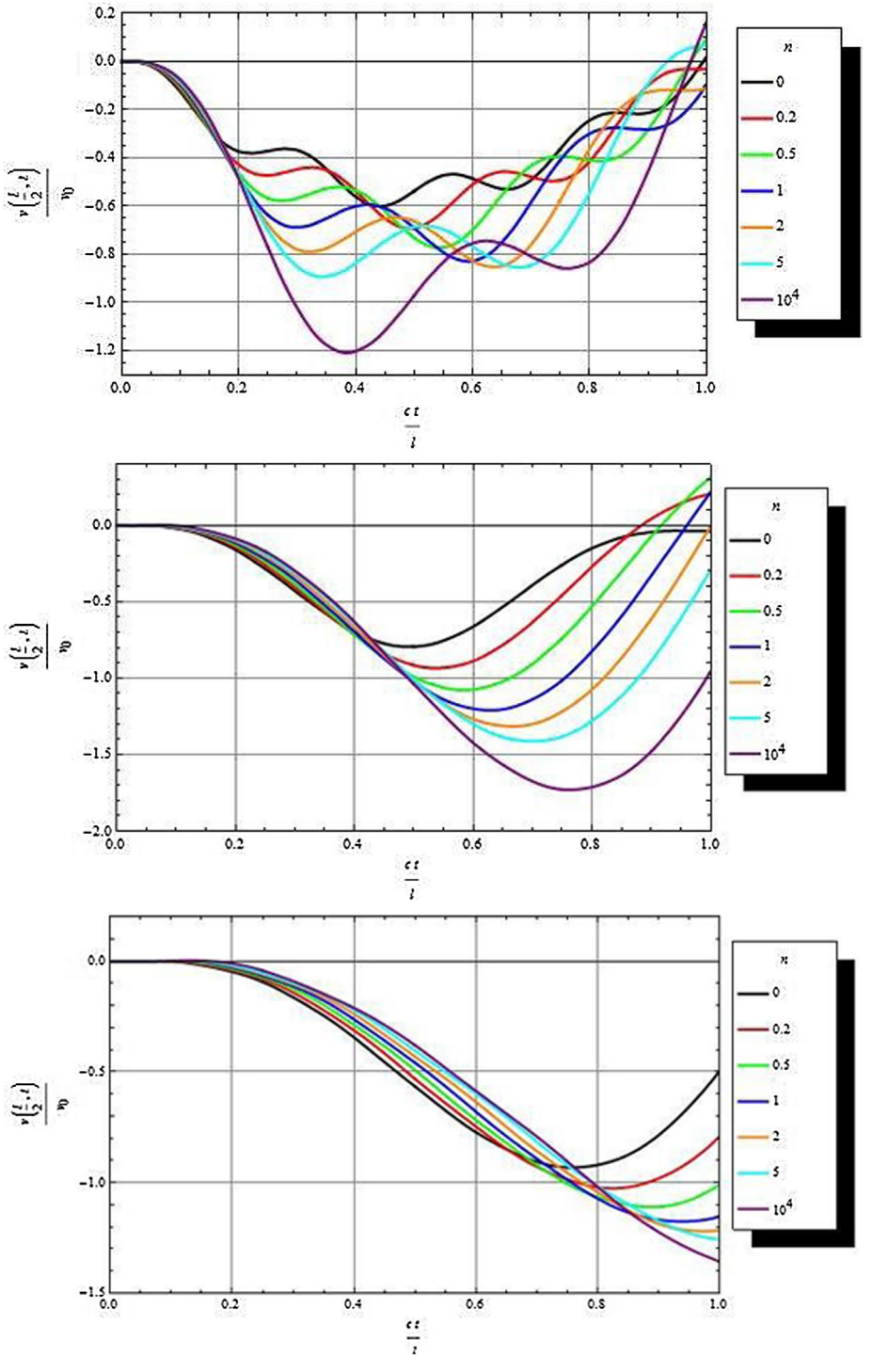

Figure 14. The non-dimensional vertical displacement at the centre of a simply supported steel-alumina FG beam for velocities (a) 50 m/s, (b) 132 m/s and (c) 250 m/s and different values of *n*.

scale of the Daubechies and BSWI wavelet families as illustrated in Figures 11 and 12, respectively. The plots demonstrate the convergence of the Daubechies and BSWI-based WFEM solutions for the non-dimensional frequencies when the order and/or the multiresolution scale are increased, particularly those associated with the higher modes of vibration.

5.2. Simply supported FG beam subjected to moving point load

The effect of the variation of the material distribution and moving load velocity on the dynamic response of a simply supported steel-alumina FG beam as well as the performance of the WFEMs are investigated. The parameters and material properties of the constituent materials of the FG beam of length l = 20 m are similar to those highlighted in Section 5.1 above and is assumed to be undamped. The governing equation describing the linear dynamic behaviour of the system is given by (Bathe, 1996):

$$[\boldsymbol{M}]\{\ddot{\boldsymbol{U}}(t)\} + [\boldsymbol{K}]\{\boldsymbol{U}(t)\} = \{\boldsymbol{F}(t)\} \tag{120}$$

where $\{\ddot{\boldsymbol{U}}(t)\}$ and $\{\boldsymbol{U}(t)\}$ represent the system acceleration and displacement vectors at time t. $\{\boldsymbol{F}(t)\}$ is the moving load vector when the moving load, of constant velocity c m s^{-1} and magnitude $p = 1 \times 10^5$ N, has travelled a distance $x_0 = ct$ over time t across the FG beam. $\{\boldsymbol{F}(t)\}$ is obtained by assembling the elemental force vectors of the system as described in Section 4. The dynamic response of the system is carried out via the Newmark time integration method with a time step of $\Delta t = 1.0 \times 10^{-5}$ s selected to ensure numerical stability and sufficient numerical accuracy of the dynamic response analysis. The deflection of the FG beam $v(x, t)$, as the moving load travels across, is normalised as a non-dimensional parameter $v(x, t)/v_0$:

$$v_0 = \frac{Pl^3}{48E_l I} \tag{121}$$

where I is the moment of inertia of the cross-section of the beam. This is the static deflection at the centre of the simply supported fully steel beam when the static load P is acting at the mid-span. The dynamic response of the beam is carried out at the centre of the beam $x = l2$, which corresponds to the position at which the maximum deflection of the beam is expected to occur. The analysis is carried out using 2 BSWI4$_3$ (37 DOFs) and 2 D12$_0$ (37 DOFs) WFEs and the results are compared with the classical FEM solution with 12 elements (39 DOFs).

The variation of the maximum normalised deflection at mid-span of the beam with respect to the moving load velocity is presented in Figure 13 for different n. The plot is for the velocity range $0 < c \leq 300$ m s^{-1} at increments of 1 m s^{-1} and the results are obtained via the BSWI4$_3$ WFEM solution. The graphical results of the Daubechies D12$_0$ WFEM and classical FEM solutions are similar to these results.

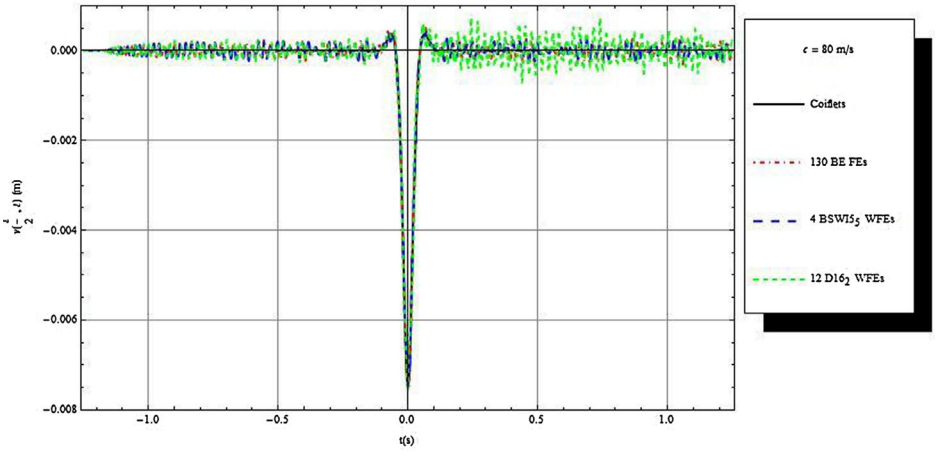

Figure 15. The vertical displacement at the centre of a simply supported steel beam on an elastic foundation (no damping) subjected to a moving point load travelling at 80 m/s.

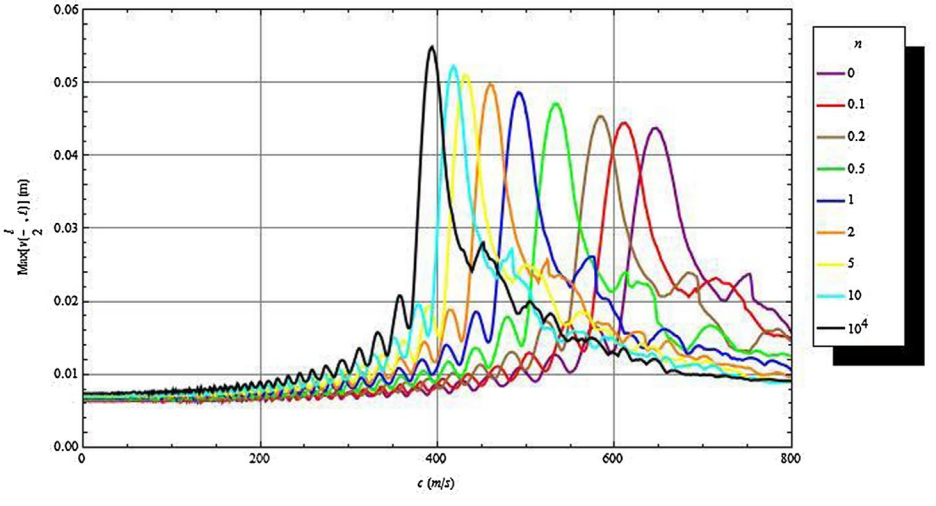

Figure 16. The variation of the maximum non-dimensional vertical displacement at the centre of a FG beam on elastic foundation with respect to moving load velocities for different *n*.

In general, the maximum non-dimensional vertical displacement at the centre of the FG beam increases as the moving load velocity increase, for all the values of *n*. However, this maximum displacement reaches a peak value which corresponds to the critical velocity of the moving load. As the velocity of the moving point load further increases (supercritical velocity), the maximum deflection at the centre of the beam begins to decrease. Therefore, the vertical displacement at the centre of the beam is significantly influenced by moving load velocity which is consistent with the findings of (Şimşek & Kocatürk, 2009).

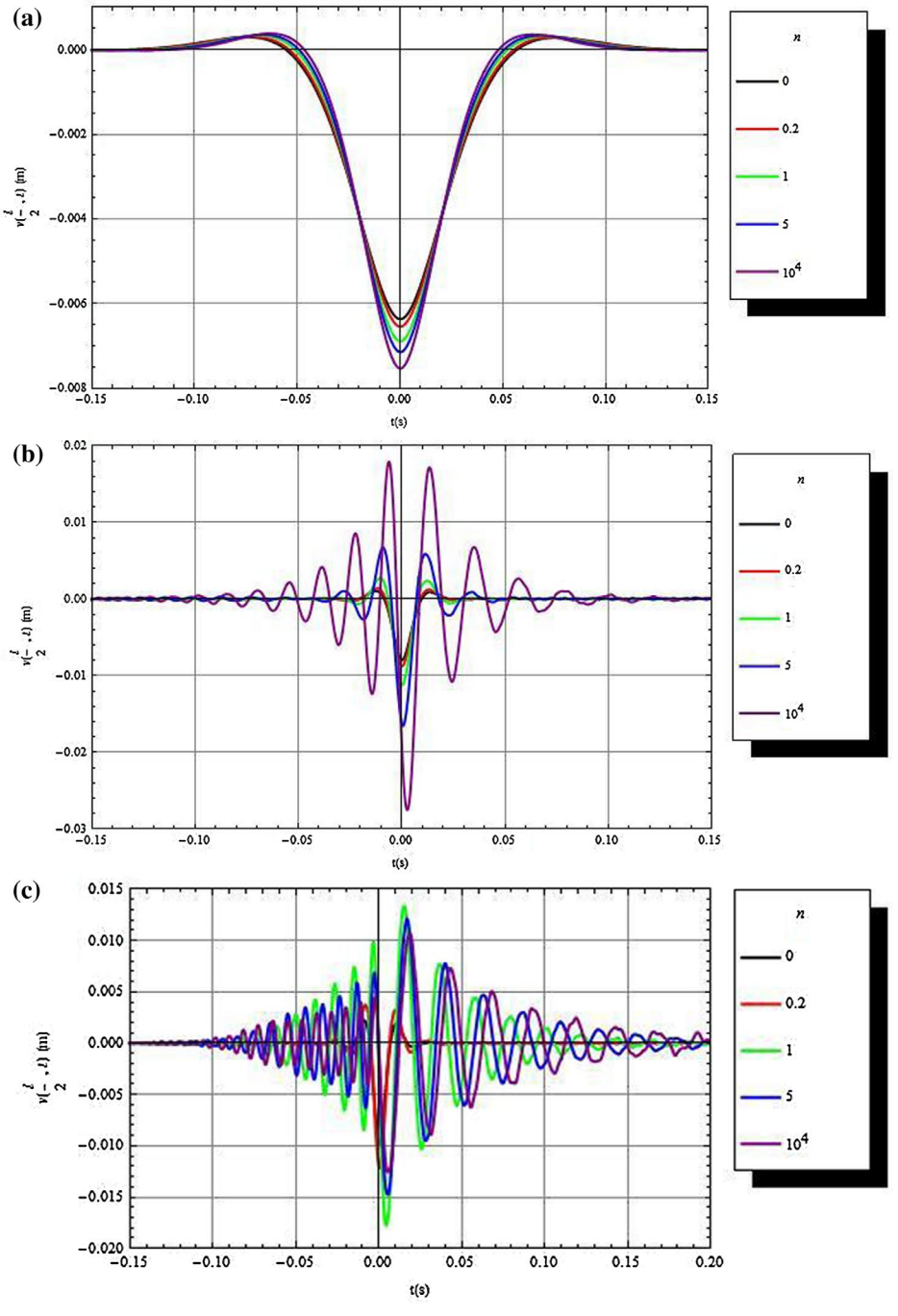

Figure 17. Vertical displacement at the centre of steel-alumina FG beam on viscoelastic foundation (5% damping) for moving load velocities (a) 80 m/s (b) 395.26 m/s and (c) 500 m/s for different values of *n*.

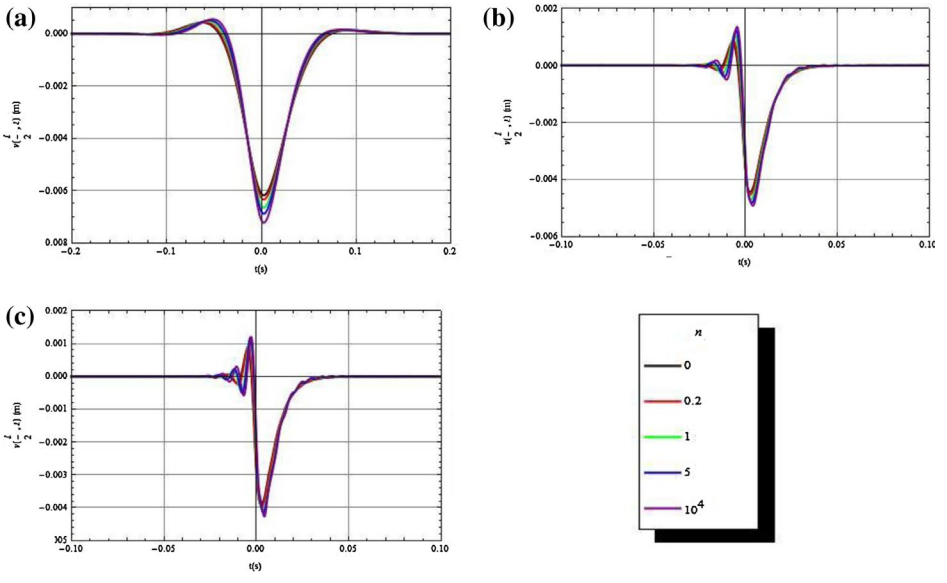

Figure 18. Vertical displacement at the centre of steel-alumina FG beam on viscoelastic foundation (100% damping) for moving load velocities (a) 80 m/s (b) 395.26 m/s and (c) 500 m/s for different values of *n*.

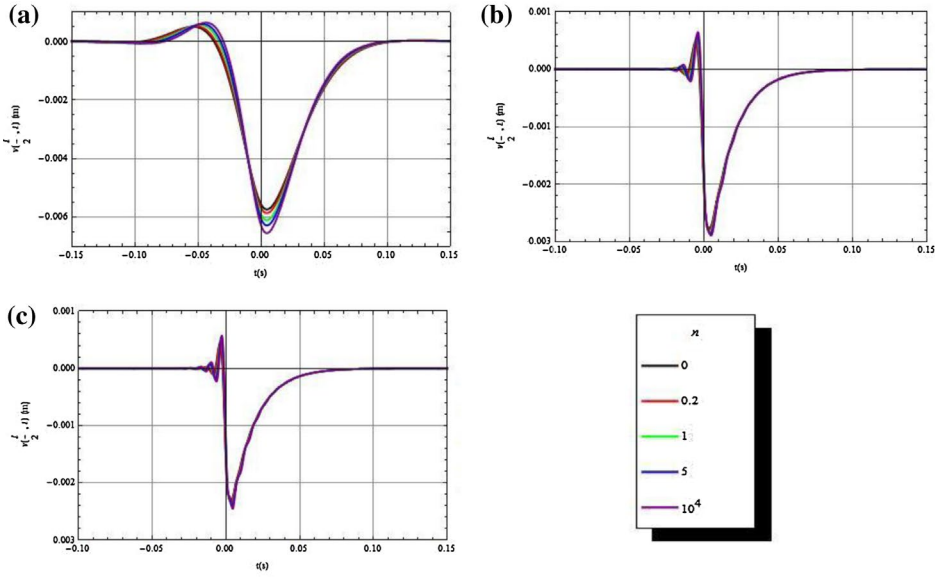

Figure 19. Vertical displacement at the centre of steel-alumina FG beam on viscoelastic foundation (100% damping) for moving load velocities (a) 80 m/s (b) 395.26 m/s and (c) 500 m/s for different values of *n*.

Furthermore, the maximum normalised deflection of the FG beam also increases as $n \to \infty$ (decrease in effective bending stiffness of the FG beam). Hence, the highest values of the maximum vertical displacement at the centre

of the beam occur when the beam is fully steel ($n = 10^4$). Therefore, the material distribution of the FG beam also significantly influences the dynamic response of the beam. Table 3 shows the critical velocities and corresponding non-dimensional maximum deflections at the centre of the FG beam for different values of n. The results presented are in relation to Figure 3. The solutions are obtained via the 12 classical FEs, 2 $D12_0$ WFEs and 2 $BSWI4_3$ WFEs formulations. The results are compared with the values obtained in Simsek and Kocaturk (indicated by "Ref.") (Şimşek & Kocatürk, 2009); the Daubechies and BSWI WFEM solutions are in very good agreement.

The non-dimensional deflection of the beam is also analysed for subcritical, critical and supercritical velocity profiles for the different values of n as illustrated in Figure 14. The velocities (a) 50 m s^{-1}, (b) 132 m s^{-1} and (c) 250 m s^{-1} are selected to represent the respective velocity profiles. The results presented are obtained using 2 $D12_0$ WFE; the BSWI WFEM and classical FEM solutions are similar.

It is important to note that the velocity profiles are based on a fully steel beam subjected to the moving point load, which has a critical moving load velocity of 132 m s^{-1}. From Figure 14, it is observed that the effect of varying the material distribution on the dynamic response of the FG beam is significant for the different velocity profiles. However, this effect decreases as the higher moving load supercritical velocities increase.

5.3. FG beam on viscoelastic foundation subjected to moving point load

The effects of the material distribution, moving load velocity and damping on the dynamic response of a simply supported steel-alumina FG beam resting on a viscoelastic foundation, as illustrated in Figure 9, are investigated in this section. The FG beam of length $l = 200$ m, moment of inertia $I = 3.055 \times 10^{-5}$ m^4, cross-sectional area $A = 7.684 \times 10^{-3}$ m^2, is subjected to a moving point load of magnitude $p = 8.34 \times 10^4$ N travelling at c m s^{-1}. The beam rests on a foundation of elastic stiffness $k_f = 3.416{\times}10^6$ N m^{-2}.

The dynamic behaviour of the system in Figure 9 is described by the governing equation:

$$\boldsymbol{M}\ddot{\boldsymbol{U}}(t) + \boldsymbol{C}\dot{\boldsymbol{U}}(t) + (\boldsymbol{K}_b + \boldsymbol{K}_f)\boldsymbol{U}(t) = \boldsymbol{F}(t) \tag{122}$$

where $\boldsymbol{M}$, $\boldsymbol{C}$, $\boldsymbol{K}_b$ and $\boldsymbol{K}_f$ are the system mass, damping, beam stiffness and foundation stiffness matrices while $\ddot{\boldsymbol{U}}(t)$,$\dot{\boldsymbol{U}}(t)$ and $\boldsymbol{U}(t)$ represent the system acceleration, velocity and displacement vectors at time t. $\boldsymbol{F}(t)$ is the moving load vector. The foundation stiffness matrix in wavelet space is evaluated as:

$$[\boldsymbol{k}_{f,e}^{w}] = \int_0^1 {}_{(1\times s)}{}^{t}\left\{\bar{\boldsymbol{\Phi}}_z{}^{j}(\xi)\right\}^{T} {}_{(1\times s)}{}^{t}\left\{\bar{\boldsymbol{\Phi}}_z{}^{j}(\xi)\right\} \mathrm{d}\xi \tag{123}$$

The wavelet space foundation stiffness matrix is also transformed into physical space via the wavelet transformation matrix and is obtained as:

$$_{(s\times s)}[\boldsymbol{k}_{f,e}^{p}] = k_f L_e \left[\boldsymbol{T}_w\right]^T [\boldsymbol{k}_{f,e}^{w}] \left[\boldsymbol{T}_w\right] \tag{124}$$

The viscous damping matrix of the foundation in wavelet space is expressed as:

$$[\boldsymbol{c}_{f,e}{}^{w}] = \int_0^1 {}_{(1\times s)}{}^{t} \left\{ \bar{\boldsymbol{\Phi}}_z{}^{j}(\xi) \right\}^T {}_{(1\times s)}{}^{t} \left\{ \bar{\boldsymbol{\Phi}}_z^{j}(\xi) \right\} \mathrm{d}\xi \tag{125}$$

and in physical space after transformation

$$_{(s\times s)}[\boldsymbol{c}_{f,e}^{p}] = dL_e \left[\boldsymbol{T}_w\right]^T [\boldsymbol{c}_{f,e}^{w}] \left[\boldsymbol{T}_w\right] \tag{126}$$

where $d = \zeta d_{cr}$ is the viscous damping coefficient, with ζ and d_{cr} denoting the damping ratio and critical damping, respectively, which is expressed as (Dimitrovová & Rodrigues, 2012):

$$d_{cr} = 2\sqrt{k_f A \rho_l} \tag{127}$$

The results obtained from 4 $BSWI5_5$ (271 DOFs) and 12 Daubechies $D16_2$ WFEs (375 DOFs) are compared with 130 classical finite elements (390 DOFs) solutions. The number of elements, order and multiresolution scales of the elements are attained when the dynamic response of a fully steel beam on a viscoelastic foundation (5% damping) converge within 3% of the exact solution for all approaches ($c = 80$ ms^{-1}) as illustrated in Figure 15.

It is observed that the BSWI WFEM solution is highly accurate with significantly less number of elements used in comparison to both the Daubechies WFEM and classical FEM. This significantly reduces the computational costs with high levels of accuracy attained. The Daubechies WFEM does not perform with similar efficiency and accuracy as the BSWI WFEM due to the numerical errors that arise from evaluating the connection coefficients.

The maximum deflection at the centre of the beam as the moving load travels at c m s^{-1} is presented in Figure 17 for different material distributions (undamped system). The plot is obtained for the velocity range $0 < c \leq 800$ m s^{-1} at increments of 1 m s^{-1} using the $BSWI5_5$ WFEM solution. The Daubechies WFEM and classical FEM plots are similar and are therefore not presented. It is observed from Figure 16 that varying the material distribution of the FG beam influences the dynamic response of the entire system for different moving load velocities. Furthermore, the moving load critical velocity value decreases as $n \to \infty$. For instance, the moving load velocity when $n = 0$ is 648 m s^{-1} and when $n = 10^4$, the corresponding critical velocity is 395 m s^{-1}.

It is known from literature that the critical velocity of a finite beam resting on an elastic foundation can be evaluated from the expression (Dimitrovová & Rodrigues, 2012):

$$c_{cr} = \frac{l}{j_{cr}\pi}\sqrt{\left(\frac{j_{cr}\pi}{l}\right)^4 \frac{EI}{\mu} + \frac{k_f}{\mu}} \tag{128}$$

where $j_{cr} = \frac{l}{\pi}\sqrt[4]{\frac{k_f}{EI}}$ is the critical mode of vibration corresponding to the lowest resonant velocity and is rounded off to the nearest integer and μ is the mass density. The critical velocity of the fully steel finite beam is obtained as 395.26 m s^{-1} via this formulation and this further validates the wavelet-based approach presented in this study.

Figures 17–19 illustrate the dynamic response at the centre of the steel-alumina FG beam resting on a viscoelastic foundation (5, 100 and 200% damping, respectively) when subjected to a moving point load for the three velocity profiles (subcritical, critical and supercritical based on a fully steel beam). It is observed from Figure 17 that the effects of varying the material distribution from $n = 10^4$ to $n = 0$ on the dynamic response at the centre of the FG beam are more significant when the moving load is travelling at a velocity approaching that of the critical velocity when the system is lightly damped. When the system is critically and supercritically damped (100 and 200% damping, respectively), the dynamic response significantly decreases, particularly for higher moving load velocities for all material distributions as observed in Figures 18 and 19. Furthermore, the introduction of damping in the system not only affects the dynamic response of the FG beam, but also influences the effect of varying n on the dynamic response. For instance, the percentage maximum deflection variation from a steel to alumina beam when subjected to a 500 m s^{-1} moving load is 21.45% when $\zeta = .05$, 8.58% when $\zeta = 1$ and 5.52% when $\zeta = 2$. Therefore, increasing damping reduces the effect of varying the material distribution on the response of the FG beam on a viscoelastic foundation.

6. Conclusions

The BSWI and Daubechies WFEMs are used to analyse the free vibration and dynamic response of a FG beam subjected to a moving point load and resting on a viscoelastic foundation. The scaling functions of the Daubechies wavelet and B-spline wavelet on the interval (BSWI) families are employed as interpolating functions for the construction of the wavelet-based FG beam elements based on Euler Bernoulli beam theory. The effect of the material distribution, moving load velocity and damping of the viscoelastic system on the dynamic response of a FG beam are investigated and discussed. Through numerical examples, it is illustrated that the WFEM solutions achieve high levels of accuracy with fewer elements implemented with respect to the classical FEM solutions in the analysis

of FG beams. This is desirable as the computational accuracy and efficiency is improved due to the multiresolution property of wavelets which enables accurate approximation of varying material distributions within FGMs and fast moving loads. Furthermore, the accuracy of the solutions can be further improved by locally increasing the order and/or multiresolution scale of the wavelet-based element. The WFEM offer vast potential to efficiently and accurately analyse more complicated systems.

Disclosure statement

No potential conflict of interest was reported by the authors.

ORCID

Cristinel Mares http://orcid.org/0000-0001-7515-9559

References

Alshorbagy, A. E., Eltaher, M. A., & Mahmoud, F. F. (2011, July). Free vibration characteristics of a functionally graded beam by finite element method. *Applied Mathematical Modelling, 35*, 412–425.

Aydogdu, M., & Taskin, V. (2007). Free vibration analysis of functionally graded beams with simply supported edges. *Materials and Design, 28*, 1651–1656.

Bathe, K. J. (1996). *Finite element procedures*. (1st ed.). New Jersey: Prentice Hall.

Chakraborty, A., Gopalakrishnan, S., & Reddy, J. N. (2003). A new beam finite element for the analysis of functionally graded materials. *International Journal of Mechanical Sciences, 45*, 519–539.

Chen, X., He, Z., Xiang, J., & Li, B. (2006). A dynamic multiscale lifting computation method using Daubechies wavelet. *Journal of Computational and Applied Mathematics, 188*, 228–245.

Chen, W.-H., & Wu, C.-W. (1995). A spline wavelets element method for frame structures vibration. *Computational Mechanics, 16*, 11–21.

Chen, X., Yang, S., Ma, J., & He, Z. (2004). The construction of wavelet finite element and its application. *Finite Elements in Analysis and Design, 40*, 541–554.

Chui, C. K., & Quak, E. (1992). Wavelets on a bound interval. *Numerical Methods in Approximation Theory, 1*, 53–75.

Daubechies, I. (1988). Orthonormal bases of compactly supported wavelets. *Communications on Pure and Applied Mathematics, 41*, 909–996.

Díaz, L. A., Martín, M. T., & Vampa, V. (2009). Daubechies wavelet beam and plate finite elements. *Finite Elements in Analysis and Design, 45*, 200–209.

Dimitrovová, Z., & Rodrigues, A. F. (2012). Critical velocity of a uniformly moving load. *Advances in Engineering Software, 50*, 44–56.

Fryba, L. (1999). *Vibration of solids and structures under moving loads* (3rd ed.). (E. Stott, Ed.) London: Thomas Telford.

He, W. Y., & Ren, W. X. (2012). Finite element analysis of beam structures based on trigonometric wavelet. *Finite Elements in Analysis and Design, 51*, 59–66.

Jha, D. K., Kant, T., & Singh, R. K. (2013, February). A critical review of recent research on functionally graded plates. *Composite Structures, 96*, 833–849.

Kadoli, R., Akhtar, K., & Ganesan, N. (2008). Static analysis of functionally graded beams using higher order shear deformation theory. *Applied Mathematical Modelling, 32*, 2509–2525.

Khalili, S. M., Jafari, A. A., & Eftekhari, S. A. (2010). A mixed Ritz-DQ method for forced vibration of functionally graded beams carrying moving loads. *Composite Structures, 92*, 2497–2511.

Ko, J., Kurdila, A. J., & Pilant, M. S. (1995). A class of finite element methods based on orthonormal, compactly supported wavelets. *Computational Mechanics, 16*, 235–244.

Koizumi, M. (1997). FGM activities in Japan. *Composites Part B: Engineering, 28*(1–2), 1–4.

Latto, A., Resnikoff, H. L., & Tenenbaum, E. (1991). The evaluation of connection coefficients of compactly supported wavelets. In Y. Maday (Ed.), *Proceedings of the French-USA Workshop on Wavelets and Turbulence*. New York, NY: Springer-Verlag.

Li, B., & Chen, X. (2014). Wavelet-based numerical analysis: A review and classification. *Finite Elements in Analysis and Design, 81*, 14–31.

Ma, J., Xue, J., Yang, S., & He, Z. (2003). A study of the construction and application of a Daubechies wavelet-based beam element. *Finite Elements in Analysis and Design, 39*, 965–975.

Pradhan, K. K., & Chakraverty, S. (2013). Free vibration of Euler and Timoshenko functionally graded beams by Rayleigh–Ritz method. *Composites Part B: Engineering, 51*, 175–184.

Quak, E., & Weyrich, N. (1994). Decomposition and reconstruction algorithms for spline wavelets on a bounded interval. *Applied and Computational Harmonic Analysis, 1*, 217–231.

Şimşek, M. (2010a). Vibration analysis of a functionally graded beam under a moving mass by using different beam theories. *Composite Structures, 92*, 904–917.

Şimşek, M. (2010b). Non-linear vibration analysis of a functionally graded Timoshenko beam under action of a moving harmonic load. *Composite Structures, 92*, 2532–2546.

Şimşek, M., & Kocatürk, T. (2009). Free and forced vibration of a functionally graded beam subjected to a concentrated moving harmonic load. *Composite Structures, 90*, 465–473.

Strang, G. (1989). Wavelet and dilation equations: A brief introduction. *Society for Industrial and Applied Mathematics Review, 31*, 614–627.

Wakashima, K., Hirano, T., & Niino, M. (1990). *Space applications of advanced structural materials*. European space agency: Proceedings of an International Symposium, (pp. 303–397), Paris, France.

Xiang, J. W., Chen, X. F., He, Z. J., & Dong, H. B. (2007). The construction of 1D wavelet finite elements for structural analysis. *Computational Mechanics, 40*, 325–339.

Yang, Z., Chen, X., Li, X., Jiang, Y., Miao, H., & He, Z. (2014). Wave motion analysis in arch structures via wavelet finite element method. *Journal of Sound and Vibration, 333*, 446–469.

Zhou, Y., Wang, J., & Zheng, X. (1998). Applications of wavelet Galerkin FEM to bending of beams and plate structures. *Applied Mathematics and Mechanics, 19*, 745–755.